1352-2310(95)00139-5

DEVELOPMENT AND APPLICATION OF A NEW AIR POLLUTION MODELING SYSTEM—PART I: GAS-PHASE SIMULATIONS

MARK Z. JACOBSON

Department of Civil Engineering, Stanford University, Stanford, CA 94305-4020, U.S.A.

RONG LU and RICHARD P. TURCO

Department of Atmospheric Sciences, University of California, Los Angeles, CA 90024-1565, U.S.A.

and

OWEN B. TOON

Space Science Division, NASA Ames Research Center, Moffett Field, CA 94035-1000, U.S.A.

Abstract—A new air pollution modeling system is discussed and applied. The system consists of GATOR, a gas, aerosol, transport, and radiation air quality model and MMTD, a mesoscale meteorological and tracer dispersion model. The gas-phase processes treated by GATOR include photochemistry, deposition, emissions, and gas-to-particle conversion. To solve stiff chemical rate equations, a sparse-matrix, vectorized Gear-type code (SMVGEAR) was used. The aerosol processes in GATOR include coagulation, aqueous chemistry, chemical equilibrium, condensational growth, dissolutional growth, evaporation, nucleation, emissions, deposition, and sedimentation. The transport processes include horizontal advection and diffusion and vertical convection and diffusion. Finally, the radiation algorithm calculates ultraviolet, visible, and infrared optical depths, mean intensities for photodissociation rates, and radiative heat fluxes for temperature calculations. The MMTD predicts winds, diffusion, temperature, pressure, humidity, soil moisture, and rainfall. These variables are fed to GATOR and radiative heating rates from GATOR are fed back to the MMTD. With the GATOR/MMTD system, gas-phase pollution was simulated for the Southern California Air Quality Study (SCAQS) days of 26–28 August 1987. Results were compared to surface measurements for many parameters. The model predicted normalized gross errors for ozone of 17.6% and 23.4% at 2:30 p.m. on the first and second days of simulation, respectively. Also, the normalized gross error during the first 12 h of simulation was 22%. Correct emissions and initial mixing ratios appear to be necessary for obtaining good results. Initial conditions outside the basin seem to affect results by the second and third days. Time-series plots, statistics, and a sensitivity test are discussed. Aerosol simulation results will be shown in a later work. Copyright © 1996 Elsevier Science Ltd

Key word index: Air quality modeling, airshed modeling, Eulerian grid modeling, gas-phase photochemistry, SCAQS data.

1. INTRODUCTION

Photochemical smog has long been a problem in the Los Angeles Basin. Major factors that cause poor air quality in the basin include emissions, gas and aerosol chemistry, gas-to-particle conversion, meteorology, and radiation. Because smog results from the interaction of several complex physical processes, a computer model is needed to simulate its formation and evolution. Some of the air pollution models in use today are variations of the Urban Airshed Model (UAM) and the California Institute of Technology (CIT) air quality model. Versions of both appear to

have branched from the same initial research (e.g. Roth et al., 1971, 1974; Reynolds et al., 1973, 1974). The UAM has since been expanded and used in numerous studies and served as the starting point of the CALGRID air quality model (Yamartino et al., 1992). Morris and Myers (1990) document the UAM, and Scheffe and Morris (1993) detail the history of the UAM. Similarly, the CIT model has co-evolved with contributions from McRae (1981), McRae et al. (1982), Russell et al. (1988a, b, 1993), Pilinis and Seinfeld (1988), Harley et al. (1993a, b), and Dabdub and Seinfeld (1994), among others. Another contemporary urban model is MARS/MEMO (Moussiopoulos et

al., 1991; Flassak and Moussiopoulos, 1992), which was initially developed to study pollution in Athens, Greece.

In this paper, a new air pollution modeling system is presented. The system consists of GATOR, a gas, aerosol, transport, and radiation air quality model (Jacobson, 1994; Jacobson and Turco, 1994, 1995; Jacobson *et al.*, 1994) and MMTD, a mesoscale meteorological and tracer dispersion model (Lu and Turco, 1993, 1994a, b). Figure 1 summarizes the processes simulated in the GATOR/MMTD system. In sum, GATOR includes treatment of gas- and aqueous-phase chemistry, condensational and dissolutional growth of aerosols, aerosol and gas dry and wet deposition, aerosol coagulation, aerosol homogeneous and heterogeneous nucleation, gas and aerosol advection, diffusion, convection, and emissions, chemical equilibrium processes, and radiative transfer. Also, the MMTD predicts winds, diffusion, pressure, temperature, humidity, soil moisture, and rainfall.

Table 1 shows the major components of the UAM, CALGRID, CIT, MARS/MEMO, and GATOR/MMTD models. All five models include gas chemistry and advection. Further, both GATOR and several versions of the CIT model include treatment of aerosols. Next, the UAM, CALGRID, and MARS models receive meteorology from off-line prognostic models while GATOR is coupled interactively to a prognostic meteorological model (MMTD) in such a way that radiation and moisture calculations from GATOR

GATOR □ / MMTD ▨
AIR POLLUTION MODELING
SYSTEM

Fig. 1. Summary of the GATOR/MMTD air pollution modeling system and the feedbacks occurring between components of the system.

can be used in the MMTD. Finally, GATOR solves for heating and photodissociation rates with a spectrally resolved radiative transfer code. The rates depend on the optical depth determined by current gas and aerosol concentrations and are calculated using different zenith angles in each horizontal grid cell. GATOR feeds the radiative heating rates back to the MMTD model to predict a component of temperature changes.

Below, the GATOR and MMTD models are briefly described. Subsequently, the setup for gas-phase simulations of pollution during the SCAQS period of 26–28 August 1987 is outlined. Finally graphical results, error analyses, a sensitivity test, and computer speeds are shown and discussed.

2. DESCRIPTION OF THE MODEL

In this section, the basic model equations are discussed. First, the continuity equation used in GATOR is described. Second, the different components are detailed. Finally, the MMTD model is summarized.

2.1. *The continuity equation for an atmospheric pollutant*

The three-dimensional continuity equation for an atmospheric pollutant can be written as (e.g. Reynolds *et al.*, 1973; Seinfeld, 1986)

$$\frac{\partial \bar{c}}{\partial t} + \frac{\partial \bar{u}\bar{c}}{\partial x} + \frac{\partial \bar{v}\bar{c}}{\partial y} + \frac{\partial \bar{w}\bar{c}}{\partial z} = \frac{\partial}{\partial x}\left(K_{xx}\frac{\partial \bar{c}}{\partial x}\right) + \frac{\partial}{\partial y}\left(K_{yy}\frac{\partial \bar{c}}{\partial y}\right)$$

$$+ \frac{\partial}{\partial z}\left(K_{zz}\frac{\partial \bar{c}}{\partial z}\right) + \sum_{i=1}^{m} R_i \quad (1)$$

where K_{xx}, K_{yy}, and K_{zz} are the diagonal terms of the eddy diffusivity tensor, u, v, and w are the east–west, north–south, and vertical wind speeds, c is concentration of the gas or aerosol, the overbar indicates a mean quantity, and R_i is the time rate of change of concentration due to the ith process (e.g. chemistry, emissions, nucleation, etc.) affecting the gas or aerosol.

Equation (1) can be generalized for several horizontal and vertical coordinate systems. For example, it may be re-written as (Toon *et al.*, 1988)

$$\frac{\partial C}{\partial t} + \frac{\partial UC}{\partial X} + \frac{\partial VC}{\partial Y} + \frac{\partial WC}{\partial Z}$$

$$= \frac{\partial}{\partial X}\left(\rho^* K_1 \frac{\partial C/\rho^*}{\partial X}\right) + \frac{\partial}{\partial Y}\left(\rho^* K_2 \frac{\partial C/\rho^*}{\partial Y}\right)$$

$$+ \frac{\partial}{\partial Z}\left(\rho^* K_3 \frac{\partial C/\rho^*}{\partial Z}\right) + VmHm_1Hm_2 \sum_{i=1}^{m} R_i \quad (2)$$

where U, V, and W are scaled wind speeds, K_1, K_2 and K_3 are scaled diffusion coefficients, X, Y, and Z are scaled coordinates, Vm, Hm_1, and Hm_2 are scaling factors for different coordinate systems, C is scaled concentration, and ρ^* is scaled air density. Equation (2) is the flux form of the scaled continuity
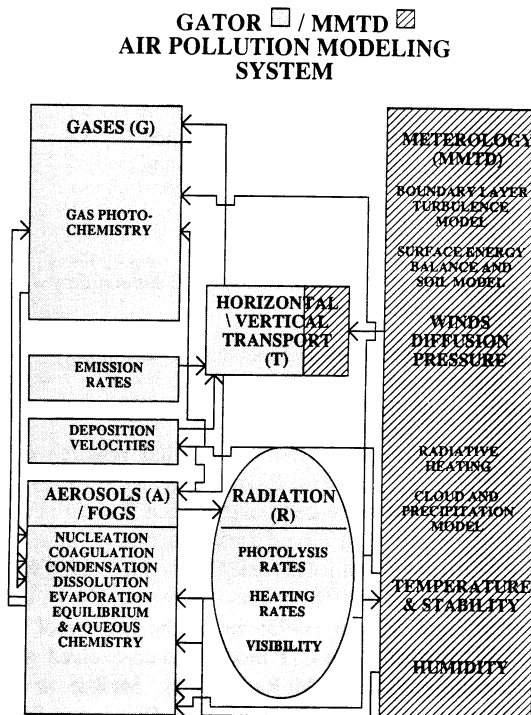
Table 1. Comparison of major components in each of five urban air pollution models

	Gas chemistry	Aerosol microphys./ chemistry	Prognostic meteorology	Advection/ diffusion	Prognostic radiative transfer
UAM	Yes	No	Yes	Yes	No
CALGRID	Yes	No	Yes	Yes	No
CIT	Yes	Yes	No	Yes	No
MARS/MEMO	Yes	No	Yes	Yes	No
GATOR/MMTD	Yes	Yes	Yes	Yes	Yes

equation for a trace gas or aerosol, and values of scaled parameters for several coordinate systems are listed in Toon et al. (1988). Horizontal coordinate systems include rectangular, lambert conformal, mercator projection, polar stereographic, global sphere projection, and non-global spherical. Vertical coordinate systems include altitude, sigma, pressure, and log pressure.

An ideal atmospheric model would solve equation (2), together with the momentum, hydrostatic, thermodynamic, water vapor continuity, and radiative transfer equations for all gas and aerosol constituents. Such a set of equations links the atmospheric variables of temperature, pressure, humidity, wind speed, wind direction, and diffusion to other factors, such as radiative heating, changes in gas and aerosol concentration, and changes in aerosol composition. In theory, such a set of equations can be solved simultaneously. However, with current computer resources, they cannot be solved over a large grid domain and for hundreds to thousands of gases plus aerosol components. Instead, for practical use, the equations are broken into a series of smaller equations. In GATOR, equation (2) is split into three one-dimensional equations (for east–west, north–south, and vertical transport) and a fourth group of equations for gas and aerosol chemical and microphysical processes. The first three equations are

$$\frac{\partial C}{\partial t} + \frac{\partial UC}{\partial X} = \frac{\partial}{\partial X}\left(\rho^* K_1 \frac{\partial C/\rho^*}{\partial X}\right) \quad (3)$$

$$\frac{\partial C}{\partial t} + \frac{\partial VC}{\partial Y} = \frac{\partial}{\partial Y}\left(\rho^* K_2 \frac{\partial C/\rho^*}{\partial Y}\right) \quad (4)$$

and

$$\frac{\partial C}{\partial t} + \frac{\partial WC}{\partial Z}$$

$$= \frac{\partial}{\partial Z}\left(\rho^* K_3 \frac{\partial C/\rho^*}{\partial Z}\right) + VmHm_1Hm_2[R_{emis}$$

$$- C(L_{fall} + L_{ddep} + L_{rain})] \quad (5)$$

where R_{emis} is the rate of emissions of either gases or aerosols (concentration s^{-1}), L_{fall} is the implicit loss rate (s^{-1}) of aerosols due to sedimentation, L_{ddep} is the implicit loss rate of gases or aerosols due to dry deposition, and L_{rain} is the implicit loss rate of gases or aerosols due to rainout. All processes described in

equations (3)–(5) apply to gases, aerosols, and aerosol components (except that gases have negligible fall velocity).

Equations (3)–(5) describe the transport of all gases and aerosols between grid cells or between model cells and boundaries. All remaining processes occur within individual grid cells. Because such process do not require information about adjacent spatial grid cells, they are not scaled. Below are the remaining generalized ordinary differential equations, which describe changes in gas number concentration, size-resolved aerosol number concentration, and size- and species-resolved aerosol volume concentration, respectively. These equations are

$$\frac{\partial \bar{c}_{G_n}}{\partial t} = R_{chem} - R_{nucg} - R_{dgrow} - R_{cgrow} \quad (6)$$

$$\frac{\partial \bar{c}_k}{\partial t} = R_{nucn} + R_{coagn} \quad (7)$$

and

$$\frac{\partial \bar{c}_{V_n k}}{\partial t} = R_{nucv} + R_{coagv} + R_{dgrow} + R_{cgrow}$$

$$+ R_{equil} + R_{aqchem} \quad (8)$$

where $\bar{c}_{G_n}$ identifies the number concentration (no. molecules cm^{-3}) of the nth gaseous component, $\bar{c}_k$ identifies the number concentration (no. particles cm^{-3}) in the kth size bin of particles, and $\bar{c}_{V_n k}$ identifies the volume concentration of the nth component (cm^3 particles cm^{-3}) in the kth size bin of particles.

In equation (6), R_{chem} is the rate of change of gas concentration due to gas-phase chemistry, R_{nucg} is the loss rate of gas due to aerosol nucleation, R_{dgrow} is the net loss (or production) rate of gas due to dissolutional growth (or evaporation) of particles, and R_{cgrow} is the net loss (or production) rate of gas due to condensational growth (or evaporation) of particles. In equation (7) R_{nucn} is the number production rate of new particles due to aerosol nucleation and R_{coagn} is the change in bin-resolved number concentration of particles due to coagulation. In equation (8) R_{nucv} is the volume production rate of new particles due to nucleation, R_{coagv} is the volume rate of change of a given component due to coagulation, R_{dgrow} and R_{cgrow} are rates of change in aerosol volume due to either dissolutional or condensational growth,

R_{equil} is the rate of change of aerosol volume due to chemical equilibrium processes, and R_{aqchem} is the rate of change of volume of a component due to aqueous chemistry.

GATOR simulates the processes described by equations (3)–(8). These processes are discussed in more detail, next.

2.2. Processes in GATOR

2.2.1. Gas-phase processes. Gas-related processes in GATOR include photochemistry, dry deposition, emissions, and gas-to-particle conversion. For photochemistry, chemical species and reactions are written into a data set. In sum, the chemical mechanism consists of inorganic reactions from Atkinson *et al.* (1992) and DeMore *et al.* (1990), organic reactions from Gery *et al.* (1989) and Atkinson *et al.* (1992), and isoprene reactions from Paulson and Seinfeld (1992) and S. Paulson (personal communication). The 218 rate equations are listed in Jacobson (1994); however, reaction rate coefficients have been updated.

To solve the first-order, ordinary differential equations for chemistry, GATOR uses SMVGEAR (Jacobson, 1994; Jacobson and Turco, 1994a). SMVGEAR derives from Gear's, predictor–corrector method (Gear, 1971), which is based on the backward differentiation formula (BDF) (e.g. Hindmarsh, 1974, 1983; Byrne *et al.*, 1977; Sherman and Hindmarsh, 1980). The BDF can be written as

$$y_n = h\beta_0 \frac{\mathrm{d}y_n}{\mathrm{d}t} + \sum_{j=1}^{q} \alpha_j y_{n-j} \qquad (9)$$

where y_n is an array of N real variables at time t_n, $\mathrm{d}y_n/\mathrm{d}t = f_n$ is an array of first derivatives for each value of y at time step n, $h = t_n - t_{n-1}$ is the value of the current time step, q is the current order of the method $(1 \leqslant q \leqslant 5)$, and α_j and β_0 are scalar multipliers $(\beta_0 > 0)$ that depend on the current order. The boundary conditions, $y(t_0) = y_0$, define the initial values for the problem.

To solve equation (9), Gear set up a predictor matrix,

$$P_n \approx I - h\beta_0 J_n \qquad (10)$$

in which I is the identity matrix and

$$J_n = J(t_n, y_n) = \left[\frac{\partial f_n^i}{\partial y_n^j} \right]_{i,j=1}^{N} \qquad (11)$$

is a Jacobian matrix of partial derivatives. With the predictor matrix, Gear solved the modified Newton iterative equation,

$$P_n[y_{n(m+1)} - y_{n(m)}] = a_n + h\beta_0 f(t_n, y_{n(m)}) - y_{n(m)} \qquad (12)$$

where m is the iteration number and

$$a_n = \sum_{j=1}^{q} \alpha_j y_{n-j}. \qquad (13)$$

By defining

$$B = a_n + h\beta_0 f(t_n, y_{n(m)}) - y_{n(m)} \qquad (14)$$

and

$$\Delta y_{n(m)} = y_{n(m+1)} - y_{n(m)} \qquad (15)$$

equation (12) reduces to

$$P_n \Delta y_{n(m)} = B. \qquad (16)$$

Gear's original code was accurate but relatively slow because it required the decomposition and back-substitution over a full matrix of partial derivatives. SMVGEAR gives the same results as Gear's original code, but is about 120 times faster when both codes are run on a Cray 90. About half the speedup of SMVGEAR was due to sparse-matrix techniques and half was due to vectorization. Additional speedups have been obtained by reordering and solving equations in grid cells with stiff chemistry together and those in grid cells with non-stiff chemistry together. Reordering is especially advantageous where sunrise and emissions occur because, at these locations, chemistry is often stiffer than at other locations.

To calculate gas dry deposition velocities in GATOR, the CIT dry deposition model (McRae *et al.*, 1982; Russell *et al.*, 1993) was implemented. The CIT model calculates the velocities using Monin–Obukhov similarity theory and detailed landuse data. For each landuse type, the model identifies surface resistance values, dependent on heating rates, for two major species, SO_2 and O_3 (Sheih *et al.*, 1986; Walcek *et al.*, 1986; Chang *et al.*, 1987). The resistances of several other species are scaled to that of SO_2. The deposition computations require information about the Monin–Obukhov (M–O) length, surface roughness lengths, and heating rates. The M–O length is calculated with the MMTD and the heating rates are calculated with the radiative transfer algorithm in GATOR.

Emissions into GATOR are discussed in Section 3.2. To calculate plume rise height for stack emissions, a subroutine by Ames *et al.* (1986) (S. Mitsutomi, personal communication) that codifies formulae from Briggs (1975) was used. Briggs gave plume rise height as a function of stack height, flowrate of emissions, exhaust temperature, wind speed, and the ambient temperature profile. In GATOR, temperature profiles and wind speeds are obtained from the MMTD. Also, stack height, exhaust temperature, and flowrate are found in the emissions inventory used, which is discussed later.

2.2.2. Aerosol processes. Aerosol processes in GATOR include emissions, nucleation, coagulation, condensational growth, evaporation, aqueous dissolution, chemical equilibrium, aqueous chemistry, sedimentation, dry and wet deposition, optical depth attenuation, and transport. These processes are described in recent work (Jacobson, 1994; Jacobson and Turco, 1995; Jacobson *et al.*, 1994) and will be discussed in more detail in later work.

2.2.3. Transport processes. In GATOR, transport is time split into east–west, north–south, and vertical

components [equations (3)–(5)]. The horizontal advection code (Pepper et al., 1979; Toon et al., 1988) uses a fourth-order in time and second order in space Galerkin technique with chapeau functions as finite elements. In brief, the code solves a tridiagonal system of equations of the form

$$
\begin{bmatrix}
B_1 & D_1 & 0 & 0 & 0 \\
A_2 & B_2 & D_2 & 0 & 0 \\
0 & A_3 & B_3 & D_3 & 0 \\
0 & 0 & A_4 & B_4 & D_4 \\
0 & 0 & 0 & A_5 & B_5
\end{bmatrix}
\begin{bmatrix}
C_1^n \\
C_2^n \\
C_3^n \\
C_4^n \\
C_5^n
\end{bmatrix}
$$
$$
=
\begin{bmatrix}
F_1 & G_1 & 0 & 0 & 0 \\
E_2 & F_2 & G_2 & 0 & 0 \\
0 & E_3 & F_3 & G_3 & 0 \\
0 & 0 & E_4 & F_4 & G_4 \\
0 & 0 & 0 & E_5 & F_5
\end{bmatrix}
\begin{bmatrix}
C_1^{n-1} \\
C_2^{n-1} \\
C_3^{n-1} \\
C_4^{n-1} \\
C_5^{n-1}
\end{bmatrix}
\tag{17}
$$

where A, B, D, E, F and G are coefficients (defined in Toon et al., 1988 and shown in Jacobson, 1994) that depend on wind speeds, diffusion coefficients, air densities, time steps, and cell sizes. Also, C is concentration, $n - 1$ is the initial time, n is the final time, and the subscripts identify grid cell numbers. The example in equation (17) is for a one-dimensional grid of length N, where $N = 5$. An advantage of the advection algorithm is that it is relatively non-diffusive. Also, since the equations form a tridiagonal matrix, they are solved quickly for thousands of gas and aerosol species. Finally, if a negative concentration occurs, mass is borrowed from adjacent grid cells. However, for the air pollution simulations shown here, hole-fitting was rarely required.

For inflow boundary conditions, a specified flux, which depends on species concentrations outside the grid domain and on the inflow wind speed, is used (Jacobson, 1994). The calculation of outside boundary concentrations is discussed in Section 3.3. For outflow boundary conditions, a chapeau condition, which results from an expansion of the Galerkin integral of the advection term by parts, is used (Toon et al., 1988).

The vertical transport scheme is described in Toon et al. (1988), who expanded on work by Turco et al. (1979) and Fiadeiro and Veronis (1977). The equations fit into a tridiagonal matrix, where the coefficients of the matrix depend on vertical wind speeds, diffusion coefficients, density differences between layers, deposition velocities, time steps, and cell thicknesses. The vertical transport code suppresses numerical diffusion using an exponential fitting scheme. Further, it prevents negative concentrations by switching from explicit to implicit coefficients if negatives are predicted to occur; however, the code is always mass-conservative. Because the equations form a tridiagonal matrix, the computer solves them quickly for thousands of gas and aerosol species.

2.2.4. *Radiative processes.* Finally, GATOR computes extinction, the radiative transfer equation, photodissociation rates, and heating rates in each grid cell. It calculates a different zenith angle in each cell using equations from the Astronomical Almanac (Nautical Almanac Office, 1993) and divides the radiation spectrum into any number of ultraviolet, visible, and infrared wavelength intervals. One advantage of calculating each photolysis rate in each grid cell as opposed to calculating each rate for an entire layer is that, during sunrise and sunset, radiation varies significantly from one end of a modeling domain to the other. For example, the sun takes approximately 15 min to appear on the west end of the Los Angeles Basin after it first appears on the east end. Thus, photolysis rates will lag on one end of the basin if a constant zenith angle is used. Also, a reason to use a radiative transfer code as opposed to look-up tables to find photolysis rates is that a radiative transfer code allows the inclusion of changing extinction coefficients. Extinction can reduce visibility to less than 10 km on a polluted day and can similarly reduce incoming radiation at most wavelengths. Thus, including changes in extinction increases the number of feedbacks that the model accounts for.

For air pollution simulations, the radiation spectrum in the model is divided into 197 wavelengths. The shortest wavelength used, $0.282\ \mu\text{m}$, is near the minimum received by the lower troposphere. For wavelengths between 0.282 and $0.8\ \mu\text{m}$, the wavelength spectrum is divided into 65 intervals of between 2.5 and $10\ \mu\text{m}$ each. For wavelengths between 0.8 and $4.3\ \mu\text{m}$, the spectrum is divided into 16 probability intervals and 61 finer wavelengths within these intervals. Finally, between 4.3 and $75\ \mu\text{m}$, the grid is divided into 18 probability intervals and 71 finer wavelengths within these intervals. Thus, a heating rate calculation requires the solution of the radiative transfer equation over all 197 intervals, and a mean intensity calculation for photorates requires the solution over the first 65 intervals.

In the model, extinction coefficients are computed to find optical depths, which are used in the radiative transfer equation. To calculate spectral extinction, scattering and absorption by gases and particles are considered. For example, Rayleigh scattering by air molecules, absorption by greenhouse gases in the infrared (Toon et al., 1989), and absorption by all gases that photodissociate (Jacobson, 1994) are included. Aerosol scattering and absorption are also included; however, these processes are not discussed here.

Optical depths above the model top are found by summing the total column amounts of ozone, water, and carbon dioxide above the top multiplied by their respective spectral cross-sections. To estimate ozone column amounts above the model top during the SCAQS period, estimates of altitude-dependent mixing ratios (Brasseur and Solomon, 1986) were combined with total ozone mapping spectrometer (TOMS) ozone data over Los Angeles for 26–28 August 1987 (NASA, 1990).

To solve the radiative transfer equation, the tridiagonal solution technique of Toon et al. (1989) is used. The radiative transfer equation can be written as

$$\mu \frac{\partial I_\lambda}{\partial \tau_\lambda}(\tau_\lambda, \mu, \phi)$$

$$= I_\lambda(\tau_\lambda, \mu, \phi) - S_\lambda(\tau_\lambda, \mu, \phi)$$

$$- \frac{\omega_{0\lambda}}{4\pi} \int_0^{2\pi} \int_{-1}^{1} P_\lambda(\mu, \mu', \phi, \phi') I_\lambda(\tau_\lambda, \mu', \phi') \mathrm{d}\mu' \mathrm{d}\phi'$$

(18)

where λ is the wavelength, θ is the zenith angle of scattering (the angle between the observed scattered intensity, I_λ, and the surface normal), $\mu = \cos\theta$, θ' is the zenith angle of incidence (the angle between the incident direction of scattering and the surface normal), $\mu' = \cos\theta'$, ϕ is the azimuthal (or longitudinal) angle of scattering, ϕ' is the azimuthal angle of incidence, τ_λ is the optical depth from the top of the atmosphere to the point of interest, measured along the zenith angle (θ), $\omega_{0\lambda}$ is the single scattering albedo, P_λ is the scattering phase function, and S_λ is the solar or infrared source function.

The solution to equation (18) gives spectrally resolved heating rates and mean intensities. From GATOR, the heating rates are fed back to the MMTD to predict part of temperature changes, and the intensities are used to calculate photodissociation rates. Absorption cross-section and quantum yield data for photodissociation were obtained from Atkinson et al. (1992), DeMore et al. (1990), and Madronich and Chatfield (personal communication).

2.3. The MMTD model

The meteorology in GATOR is driven by the mesoscale meteorological and tracer dispersion (MMTD) model (Lu and Turco, 1993, 1994a, b). The MMTD is a hydrostatic, finite difference prognostic model that uses sigma coordinates in the vertical and spherical coordinates in the horizontal. It predicts horizontal and vertical wind speeds and directions, vertical diffusion coefficients, turbulent free convection, temperature, pressure, humidity, changes in soil moisture, and cloud liquid water content. Further, the temperature profile it predicts is used to calculate atmospheric stability and the boundary layer height. The MMTD has successfully predicted elevated layers of pollution, similar to those detected in lidar images by Wakimoto and McElroy (1986).

To compute the variables listed above, the MMTD solves the primitive equations, which include the momentum, thermodynamic, continuity, hydrostatic, and water vapor mass continuity equations. The forms of these equations as used in the MMTD are detailed in Lu and Turco (1994a).

While the MMTD feeds winds, diffusion coefficients, convective mass transfer rates, pressure, temperature, and humidity to GATOR, GATOR cal-

culates radiative heating rates for the MMTD. The MMTD uses radiative heating rates to calculate part of the diabatic temperature change.

3. SETUP OF MODEL SIMULATIONS

To test the validity of the GATOR/MMTD system, results were compared to observations gathered from the Los Angeles Basin during the SCAQS period of 26–28 August 1987. Here, the model setup for gas-phase simulations is discussed.

3.1. Ambient data for comparisons

The period 26–28 August 1987 was chosen for model validation because the number of ambient measurements was large and a detailed California Air Resources Board emissions inventory was created for this period. Lawson (1990) describes the data-gathering that occurred during the SCAQS.

To validate the GATOR/MMTD model, several SCAQS data sets were used. First, the SCAQS modeling archive (King et al., 1990; B. Croes and California Air Resources Board, personal communication) was used for initializing model parameters and comparing predictions against. The archive contains surface mixing ratios of ambient ozone, carbon monoxide, nitrogen dioxide, nitric oxide, sulfur dioxide, non-methane hydrocarbons (NMHCs), and methane, measured at 56 monitoring sites during the period 27–30 August 1987. The archive also contains surface data for temperature, dew point, relative humidity, sea level pressure, wind speed, wind direction, visibility, cloud cover, ceiling height, sea surface temperature, precipitation, solar radiation, and standard deviation of wind direction. At least one variable was measured at each of 98 sites. Finally, the archive contains upper air data for pressure, temperature, dew point, relative humidity, wind speed, and wind direction, taken from 257 soundings measured at 15 locations.

In addition, SCAQS organic gas data from nine sites in the Los Angeles Basin were used (Lurmann et al., 1992; B. Croes, personal communication). From the data, individual gases were combined into bond groups or kept as separate species that could be used in the Carbon Bond IV-EX mechanism. Such species and bond groups included formaldehyde (FORM), ethene (ETH), higher molecular weight aldehydes (ALD2), carbons bonded by a single bond (PAR), carbons bonded by a double bond (OLE), acetone (AONE), other ketones (KET), seven-carbon aromatics (TOL), eight-carbon aromatics (XYL), and isoprene (ISOP). Other gas data used for comparison were measurements of nitrous acid and formaldehyde (Winer et al., 1989; Winer and Biermann, 1994), formaldehyde (Mackay et al., 1988), and peroxyacetyl nitrate (Williams and Grosjean, 1989).

3.2. Emissions data

Emissions data for Wednesday, 26 August–Friday, 28 August 1987 were supplied by the California Air Resources Board (Allen and Wagner, 1992; P. Allen, personal communication). The emissions grid covers a region 325 km east–west by 180 km north–south, with the southeast corner at 33°8'35" N latitude and − 119°24'44"E longitude. The gas data in the inventory include hourly gridded emissions of NO_x, oxides of sulfur (SO_x), organic gases, and carbon monoxide. NO_x is partitioned into NO, NO_2, and HONO; SO_x is partitioned into SO_2 and SO_3; and organic gases are divided into both individual species and bond groups. The individual species include formaldehyde, methanol, ethene, ethanol, acetone, and methane, and the bond groups include ALD2, PAR, OLE, KET, TOL, XYL, and ISOP.

While the CARB emissions inventory is detailed, some emission estimates appear to be low. For example, Ingalls et al. (1989) concluded from a tunnel study that mobile hot-exhaust emissions of carbon monoxide and reactive organic gases were 2.1–3.6 and 1.8–6.9 times higher, respectively, than originally estimated. Using this information, Harley et al. (1993a) assumed that mobile hot exhaust emissions of carbon monoxide and reactive organic gases were 3.0 times original EMFAC7E values. Similarly, Pierson et al. (1992) concluded that mobile hot exhaust emissions of CO and ROGs were 2.7 and 4.0 times higher, respectively, than EMFAC7C values. For the simulations presented here, ROG hot exhaust emissions (EMFAC7C) were initially multiplied by a factor of 3.0. In a sensitivity study, the emissions were multiplied by a factor of 4.0. On-road vehicle organic hot exhaust represents about 17% of all organic emissions (Harley et al., 1993a). For all simulations, CO hot exhaust emissions were multiplied by a factor of 2.7.

In addition, the CARB emissions inventory separates stack from other gas emissions. Table 2 shows the relative rate of stack compared to non-stack emissions for the adjusted inventory of 27 August 1987. In sum, about 0.2% of CO emissions, 7.2% of NO_x emissions, 12% of SO_x emissions, and 0.3% of ROG emissions originated from stacks.

3.3. Additional data

In addition to ambient and emissions data, other data were used to initialize and define parameters in GATOR. These included topographical data from the U.S. Geological Survey and landuse, surface roughness, soil albedo, soil moisture, soil density, and soil heat capacity data from the South Coast Air Quality Management District (SCAQMD) (J. Lestor, personal communication).

Further, because most gridded data — including data for emissions, landuse, surface roughness length, soil wetness, soil density, soil specific heat, and albedo — were designed for a universal transverse mercator (UTM) grid projection, the data were interpolated to spherical (geographic) coordinates. UTM grid cells cross geographic cells at random locations. Thus, to interpolate, the area of UTM cell lying in a geographic cell was physically integrated, as described next.

Table 2. Comparison of non-stack to stack emissions for 27 August 1987, using an adjusted EMFAC7C SCAQS emissions inventory (Allen and Wagner, 1992)

	Non-stack	Stack	Total
Inorganics $(t\ d^{-1})$			
Carbon monoxide (CO)	9773	23	9796
Nitric oxide (NO)	700	54	754
Nitrogen dioxide (NO_2)	120	9	129
Nitrous acid (HONO)	6	0.5	6.5
Sulfur dioxide (SO_2)	96	13	109
Sulfur trioxide (SO_3)	4	0.5	4.5
Organics $(10^6\ mol\ d^{-1})$			
Methane (CH_4)	56	0.3	56.3
Paraffins (PAR)	88	0.3	88.3
Ethene (ETH)	5.2	≪1	5.2
Olefins (OLE)	3.5	≪1	3.5
Formaldehyde (HCHO)	1.2	≪1	1.2
C_2 + aldehydes (ALD2)	1.4	≪1	1.4
Methanol (MEOH)	0.2	≪1	0.2
Ethanol (ETOH)	0.6	≪1	0.6
Acetone (AONE)	0.4	≪1	0.4
Other ketones (KET)	0.1	≪1	0.1
Toluene (TOL)	2.6	≪1	2.6
Xylene (XYL)	1.9	≪1	1.9
Isoprene (ISOP)	0.8	0	0.8
Other unreactive	15	< 1	15

Note. To obtain the adjustments, mobile hot exhaust emissions of carbon monoxide and organic gases were multiplied by factors of 2.7 and 3.0, respectively.

To integrate, each UTM grid cell (usually 5×5 km in area) was divided into 10,000 or more smaller cells (each 50×50 m in area). Each smaller cell was assumed to contain the same data values as the larger UTM cell it was partitioned from. Next, the latitudes and longitudes of the four corners of each smaller cell were located using UTM to geographic conversion data and formulae (U.S. Department of the Army, 1958). Subsequently, for each large UTM cell (U), the number of smaller UTM cells ($N_{U,G}$) in each geographic cell (G), was counted. Consequently, either the cumulative (S_G—for emissions) or average (V_G — for all other cases) datum value in each geographic cell was calculated from

$$S_G = \sum_{U=1}^{M_G} \left(\frac{N_{U,G} A_S D_U}{A_U} \right) \tag{19}$$

or

$$V_G = \frac{\sum_{U=1}^{M_G} (N_{U,G} A_S D_U)}{A_G} \tag{20}$$

where M_G is the number of large UTM cells touching geographic cell G, A_S is the area of a small UTM cell, A_U is the area of a large UTM cell, A_G is the areas of a geographic cell, and D_U is the original datum value in a large UTM cell. The precision of this method increases when smaller and smaller mini-UTM cells are used.

3.4. Initializing variables

Before each simulation, meteorological parameters, gas mixing ratios, and model grids were initialized. GATOR and the MMTD are coupled together; but GATOR may nest horizontally and vertically within the MMTD. In the horizontal, GATOR maintains the same grid spacing as the MMTD; however, the lateral boundaries of GATOR may lie within or directly upon the boundaries of the MMTD. In the vertical MMTD layers can either match GATOR layers or nest within them. Thus, the number of MMTD layers within each GATOR layer is greater than or equal to one. For the simulations discussed herein, both GATOR and the MMTD used spherical coordinates.

Figure 2 shows a diagram of the Los Angeles Basin. While the Pacific Ocean borders the western edge, the Santa Monica, San Gabriel, San Bernardino, and Santa Ana Mountains either surround or intersect the basin. Also, passes, such as Cajon and Banning in the San Bernardino Mountains and Tejon in the Tehachapi Mountains (not shown in Fig. 2) provide narrow passages for some flow into and out of the basin.

To initialize the model coordinate system, the southwest corner of the MMTD was placed at 33.06°N latitude and 119.1°W longitude. The uniform grid-spacing was 0.05° east–west (about 4.6 km) and 0.045° north–south (about 5.0 km), and the model

dimension was 55 east–west grid cells by 38 north–south cells by 20 vertical sigma layers. Each edge of GATOR was placed two grid cells within each edge of the MMTD in order to reduce the effects of boundary wind values calculated by the MMTD. However, the horizontal grid spacing in GATOR and the MMTD were the same. Thus, GATOR consisted of 51 east–west cells by 34 north–south cells, with a southwest corner at 33.15°N latitude and 119.0°W longitude.

Further, while 20 vertical levels were used for the MMTD, 14 were used for GATOR in order to reduce computational time. These layers included the same bottom eight of the MMTD plus six more, each encompassing two MMTD layers. To obtain values for meteorological parameters in each of the six upper layers, the values from the two corresponding MMTD layers were averaged. The top in both models was set to 250 mb. The eight lowest layers (the same in both models) were all below about 850 mb (about 1.5 km). In sum, the MMTD solved equations in 41,800 grid cells while GATOR solved in 24,276 cells. All horizontal and vertical dimensions in each model are changeable.

Next, meteorological parameters were initialized with interpolated SCAQS sounding data (King *et al.*, 1990). The data included information about pressure, temperature, dew point, wind speed, and wind direction at numerous altitudes. All simulations started at 4:30 a.m. PDT on 26 August 1987. Since no sounding occurred at either of these times, all soundings that occurred between 4:00 and 6:00 a.m. PDT each day were interpolated. Three such soundings were taken on 26 August. All winds were initialized with zero velocity to ensure mass conservation and to avoid startup waves near mountain regions. Finally, initial sea-surface temperatures (SSTs) were interpolated for each grid cell from four SCAQS buoy data points. Each hour of the model run, SSTs were re-interpolated. SSTs averaged between 16 and 17°C.

In addition, initial gas mixing ratios were initialized in several stages. First, the mixing ratios of several species were set to free tropospheric values. In the case of nitric oxide, vertical profiles from Drummond *et al.* (1988) were used; for ozone, profiles measured by Marenco and Said (1989) were used; for carbon monoxide and methane, profiles were obtained from Marenco *et al.* (1989); for ethene, surface data from Singh *et al.* (1988) and upper air data from Bonsang *et al.* (1991) were used; for nitric acid, a profile suggested by Brasseur and Solomon (1986) was used.

Next, surface mixing ratios of NO, NO_2, O_3, CH_4, CO, SO_2, H_2O, CH_2O, ALD_2, PAR, OLE, AONE, KET, TOL, XYL, and ISOP were horizontally interpolated from available SCAQS data for 4:30 a.m. PDT on 26 August 1987. Since detailed NMOC data were not available for that day, NMOC data for 6:00 a.m. PST on 26 August were used because they were the cleanest of the three morning hours of NMOC data considered (27–29 August). All interpo-
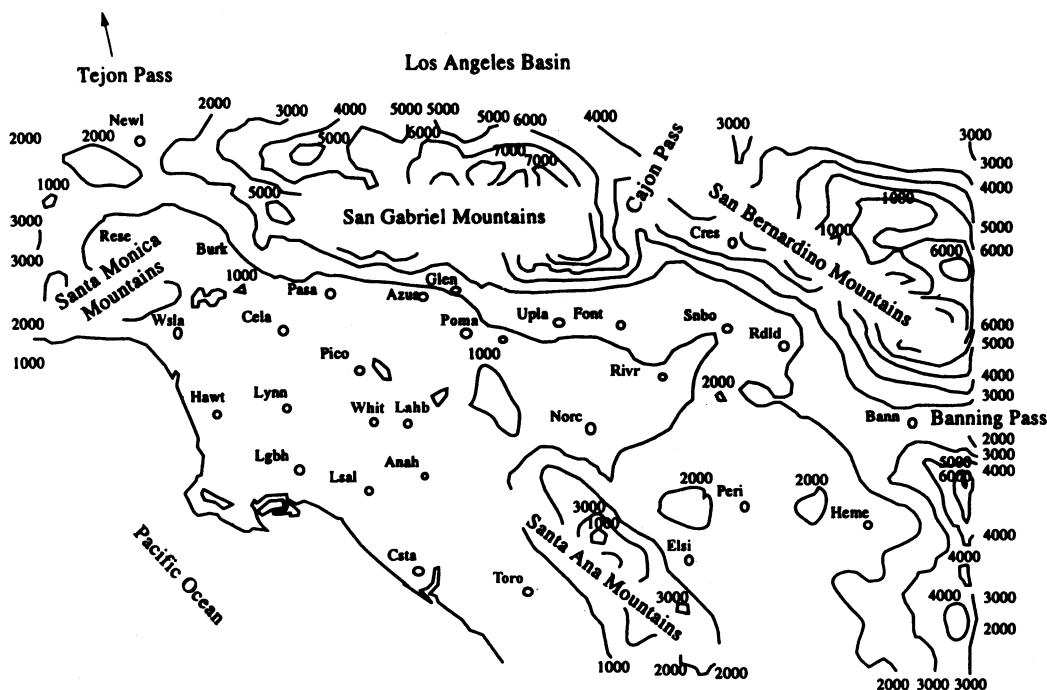
Fig. 2. Topographical map of the Los Angeles Basin showing the location of several air quality monitoring sites. The numbers are elevation, in feet and each four-letter symbol identifies a station site. The sites are Newhall (NEWL), Reseda (RESE), West Los Angeles (WSLA), Burbank (BURK), Los Angeles (CELA), Hawthorne (HAWT), Lynwood (LYNN), Pasadena (PASA), Pico Rivera (PICO), Long Beach (LGBH), Azusa (AZUS), Glendora (GLEN), Whittier (WHIT), La Habra (LAHB), Los Alamitos (LSAL), Anaheim (ANAH), Costa Mesa (CSTA), Pomona (POMA), El Toro (TORO), Upland (UPLA), Fontana (FONT), Norco (NORC), Riverside (RIVR), Crestine (CRES), San Bernardino (SNBO), Redlands (RDLD), Perris (PERI), Elsinore (ELSI), Hemet (HEME), and Banning (BANN). Not shown are Thousand Oaks (THSO—west of Reseda), Simi Valley (SIMI—north of Thousand Oaks), Oceanside (OSDE—along the coast, south of Costa Mesa), Victorville (VCTC—north of Fontana in the San Gabriel Mountains), Palm Springs (east of Banning), Claremont (CLAR—east of Azusa), Long Beach City College (LBCC—in Long Beach), CM44 (in Riverside), and CM62 (near Temecula, in the south basin), among others.

lated surface mixing ratios were assumed constant up through the morning inversion. Above this height and outside the interpolation domain of influence, the mixing ratios of these species were set to the background values.

Finally, the modeling system used the following time-splitting time intervals: (a) SMVGEAR chemistry was solved using 900-s intervals, during which integration time steps varied between < 0.00001 and 900 s, (b) MMTD variables were solved using 6-s time intervals, (c) horizontal and vertical transport were solved using 300-s intervals (meteorological variables for the interval were calculated by averaging MMTD values over the 300-s interval), and (d) radiation was solved using 900-s intervals (photorates for chemistry were interpolated between values from the beginning and end, respectively, of a radiation interval).

3.5. Boundary conditions

The horizontal inflow boundary condition described in Section 2.2.3 requires time-dependent mixing ratios of gases beyond the boundary. Mixing ratios of each gas were initialized in four distinct

columns, each containing the same number of layers as GATOR. For each layer, the outside mixing ratio was initialized with the mixing ratio from the inside center grid cell for each lateral boundary. Since outside boundary mixing ratios vary significantly during the day due to chemistry, chemical equations in each outside boundary cell were continuously solved for with SMVGEAR. Consequently, mixing ratios of gases outside the boundaries followed diurnal patterns similar to those of free tropospheric gases.

At the model top (250 mb, or about 10.3 km), no gases were permitted to escape or enter. Since data at the surface were being compared over a short time period (one to three days), this assumption may be reasonable. However, GATOR does permit inflow and outflow from the top, and the top can be extended to any pressure level.

3.6. Error checks

To determine model performance, error checks were performed. These included checks for mean absolute normalized gross error, normalized bias, paired peak estimation accuracy, and temporally paired

peak estimation accuracy (Tesche, 1988; DaMassa et al., 1992). The normalized gross error written as

$$NGE = \frac{1}{N_S} \sum_{i=1}^{N_s} \frac{|P_{x_i t} - O_{x_i t}|}{O_{x_i t}} \qquad (21)$$

compares the absolute value of model to observed mixing ratio of a given species, summed and averaged over all observations. In equation (21), N_S is the number of observation sites, P is the predicted value, O is the observed value, x_i is the location of site i and t is the time. For NGE, all observations and predictions are paired in space and time. The normalized bias (NB) is the same as the gross error, except no absolute value is considered. Next, the paired peak accuracy identifies how well the model predicts the peak observed mixing ratio at the time and location of the peak. Thus,

$$PPA = \frac{P_{\hat{x}_i t} - O_{\hat{x}_i t}}{O_{\hat{x}_i t}} \qquad (22)$$

where the hats indicate values at the time and location of the peak observed value. Finally, the temporally paired peak accuracy identifies how well the model predicts the peak observed mixing ratio at the same time of the peak, but at any other location. Thus,

$$TPPA = \frac{P_{x_i t} - O_{x_i t}}{O_{x_i t}}. \qquad (23)$$

While actual station data were used to determine observed values, bilinear interpolation (e.g. Press et al., 1993) of four surrounding grid cell centers was used to determine model variable values at the stations.

4. MODEL RESULTS

Next, model results are compared to observations for cases where no aerosol-phase processes were included in the model simulations. To obtain these results, a three-day simulation was run from 4:30 a.m. PDT 26 August to 0:30 a.m. PDT 29 August 1987. In addition, results from a sensitivity analysis are shown for a case where the hot exhaust organic gas emission factor was increased from 3.0 to 4.0. Additional sensitivity analyses were performed, and their results are discussed.

First, the results of GATOR/MMTD performance tests are shown in Tables 3–6. Table 3 shows gross error and normalized bias for both the first 12-h period and the entire 68-h period of the simulation. To obtain these results, normalized gross errors and biases were tabulated over either the 12- or 68-h time periods. Tables 4–6 show statistics for 14:30 on 26, 27 and 28 August respectively. Column two in all tables is the number of station observations for which data (above a cutoff level) were available at the time of day, column three is the mean absolute normalized gross error, and column four is the normalized bias. For Tables 4–6, column five is the name of the SCAQMD station where the observed peak parameter value at the time of day occurred, column six is the model error at that time and location, column seven is the distance from the observed peak value where the model peak value occurred, and column eight is the difference in model vs observed peak value. The gross errors and biases for ozone, nitric oxide, and nitrogen dioxide were calculated using cutoff values of

Table 3

Parameter	No. of observations	Gross error (%)	Bias (%)
12-h average from 4:30–16:30, 26 August			
O_3	307	22.0	− 2.3
NO	131	53.3	− 23.3
NO_2	297	39.2	− 10.9
NO_x	306	41.5	− 14.4
CO	297	32.4	− 14.3
CH_4	67	9.4	− 1.3
SO_2	97	25.5	2.4
Temp.	176	0.67	− 0.18
Rel. Hum.	103	28.3	28.0
Wind Drct.	429	12.4	1.2
Wind Spd.	323	53.2	0.5
68-h average from 4:30, 26 August–0:30, 29 August			
O_3	1244	32.6	− 3.5
NO	541	68.9	3.9
NO_2	1451	52.2	− 6.5
NO_x	1560	61.3	3.5
CO	297	51.4	2.1
CH_4	335	12.0	0.5
SO_2	455	39.6	− 26.4
Temp.	958	0.80	− 0.4
Rel. Hum.	549	24.1	13.6
Wind Drct.	2277	13.6	0.8
Wind Spd.	1746	74.5	41.8

Table 4

14:30, 26 August.

Parameter	No. of observations	Gross error (%)	Bias (%)	Location of observed peak	Model error at location of observed peak (%)	Distance of model peak from observed peak (km)	Difference between model and observed peak (%)
O_3	37	17.6	-0.83	RIVR	-17.7	35.7	43.7
NO	1	50.9	-50.9	LYNN	-64.8	30.2	-12.2
NO_2	19	45.9	-41.4	AZUS	-52.2	17.2	-5.6
NO_x	23	43.6	-35.0	—	—	—	—
CO	19	33.1	-24.2	RIVM	-80.3	34.5	-32.8
CH_4	5	2.7	-0.5	CELA	-4.2	—	—
SO_2	5	27.7	-11.8	LBCC	-1.8	12.0	26.5
HCHO	1	25.6	25.6	—	—	—	—
Temp.	14	0.88	-0.19	UPLA	-1.8	—	—
Rel. Hum.	8	42.2	42.2	HAWT	8.6	—	—
Wind Drct.	33	8.1	-2.2	—	—	—	—
Wind Spd.	33	43.7	19.7	SIMI	-57.9	—	—
Solar Rad.	2	5.2	1.3	—	—	—	—

4, 2, and 2 pphm, respectively (DaMassa *et al.*, 1992). Other cutoffs used were 2 pphm for NO_x, CO, CH_4, and NMOC; 1 pphm for PAR; 5 pphb for SO_2; and 0.1 ppb for all other organics. Cutoffs were not used for other parameters. A(—) indicates that either this value was not calculated (in the cases of NO_x and Wind Drct.) or the number of stations for this parameter was fewer than four (all other cases).

On the other hand Figs 3–60 show time-series comparisons of predicted to observed mixing ratios, temperatures, humidities, and wind speeds at different locations throughout the South Coast Air Basin. The simulation period was Wednesday, 26 August 4:30 a.m. PDT to Saturday, 29 August 0:30 a.m. PDT, 1987. *Hour After First Midnight* means the Pacific Daylight Time hour after 0:00 a.m. on the first day of simulation. The resolutions of CO and SO_2 observational data are 1 and 0.01 ppmv, respectively. All organic mixing ratios are shown in ppmv for the species or bond group, not ppb-C. Figures 11–13, and 31 show results of the sensitivity study in addition to the baseline comparison of model results to data. In those plots, *Predicted* 3.0 refers to the baseline simulation, where organic hot exhaust emissions where multiplied by a factor of 3.0, and *Predicted* 4.0 refers to results obtained by multiplying organic hot exhaust emissions by a factor of 4.0.

4.1. Ozone

Table 3 shows that, for the first 12 h, the normalized gross error in ozone mixing ratios was 22%, calculated from 307 comparisons of predictions to station readings. Tables 4–6 show statistics for 2:30 p.m. PDT, 26, 27 and 28 August respectively. Table 4 shows that the ozone gross error at 2:30 p.m. was 17.6%. Table 4 also shows that the highest observed mixing ratio of ozone in the basin at 2:30 p.m. on 26 August was at Riverside. The predicted mixing ratio at that location was 17.7% lower than the observation. On subsequent days, the gross error for ozone increased. For example, the gross errors at 2:30 p.m. on 27 and 28 August were 23.4 and 33.1%, respectively (Tables 5 and 6). Further, Table 3 shows that the gross error for ozone, averaged over the entire 68-h simulation period (including both day and night), was 32.6%. Thus, ozone predictions were best early in the simulation.

Figures 3–14 show three-day time-series plots of ozone mixing ratios at several locations scattered throughout the basin. The plots indicate that, despite statistics showing the increase in mixing ratio gross error over time, mixing ratios at several individual locations improved or stayed constant throughout the simulation period. In some cases, peak mixing ratios did not decrease; instead, the times of the peak mixing ratios were delayed or advanced. For example, Figs 3–5 show that the times of peak ozone mixing ratios in the San Fernando Valley and beyond were either slightly delayed or advanced by the third day of simulation. In coastal areas (Figs 6–8), mixing ratio

Table 5

Parameter	No. of observations	Gross error (%)	Bias (%)	Location of observed peak	Model error at location of observed peak (%)	Distance of model peak from observed peak (km)	Difference between model and observed peak (%)
O_3	35	23.4	−7.3	CLAR	−29.3	14.3	4.4
NO	2	21.4	−13.1	LBCC	−3.2	3.6	3.1
NO_2	20	48.1	−38.7	AZUS	−65.3	19.4	−28.9
NO_x	22	40.2	−33.1	—	—	—	—
CO	21	43.5	−21.7	RIVM	−78.8	90.1	−29.4
CH_4	6	13.2	8.2	CLAR	−3.6	—	—
SO_2	5	35.6	−35.6	LBCC	−37.2	1.2	35.8
PAN	6	29.7	−15.2	CLAR	−57.4	—	—
HCHO	2	6.5	−2.4	—	—	—	—
PAR	2	30.1	−30.1	—	—	—	—
ETH	2	16.7	−9.1	—	—	—	—
NMOC	2	42.6	−42.6	—	—	—	—
Temp.	14	1.3	−0.2	UPLA	−2.3	—	—
Rel. Hum.	8	48.4	46.7	HAWT	−4.1	—	—
Wind. Drct.	33	10.0	1.3	—	—	—	—
Wind Spd.	33	39.0	9.1	SIMI	−46.6	—	—
Solar Rad.	2	4.4	4.4	—	—	—	—

14:30, 27 August.

page 13 of 25

Table 6

Parameter	No. of observations	Gross error (%)	Bias (%)	Location of observed peak	Model error at location of observed peak (%)	Distance of model peak from observed peak (km)	Difference between model and observed peak (%)
O_3	37	33.1	−26.6	GLEN	−56.1	32.7	0.2
NO	2	60.9	−69.9	LGBH	−30.1	21.3	65.2
NO_2	20	59.7	−40.9	POMA	−78.7	61.0	−11.8
NO_x	24	58.3	−28.6	—	—	—	—
CO	21	48.6	−43.9	AZUS	−54.4	48.1	0.2
CH_4	6	10.9	5.2	CLAR	1.7	—	—
SO_2	9	52.3	−51.7	LBCC	−70.2	20.0	−17.2
PAN	6	73.8	−73.8	CLAR	−72.1	—	—
HCHO	2	38.5	−38.5	—	—	—	—
PAR	2	67.5	−67.5	—	—	—	—
ETH	2	18.8	−6.0	—	—	—	—
NMOC	2	63.2	−63.2	—	—	—	—
Temp.	14	1.5	−0.1	UPLA	−1.9	—	—
Rel. Hum.	8	34.1	21.5	HAWT	−15.9	—	—
Wind. Drct.	33	11.1	−2.3	—	—	—	—
Wind Spd.	33	44.4	11.5	BANN	−20.6	—	—
Solar Rad.	2	4.7	4.7	—	—	—	—

14:30, 28 August.
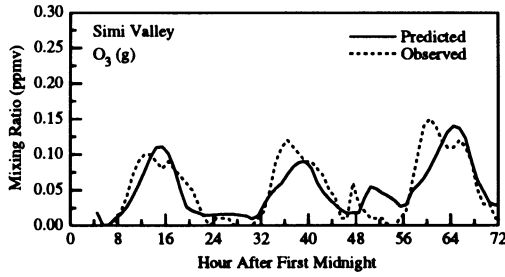
Fig. 3.
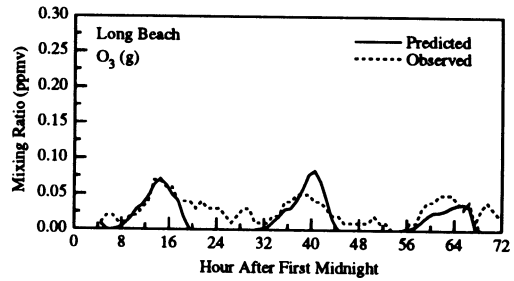

Fig. 7.
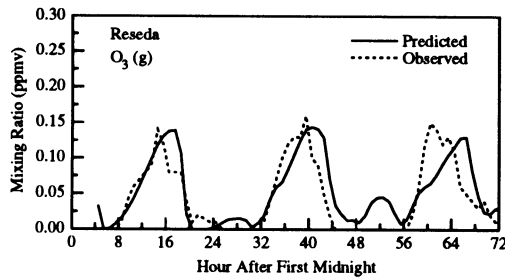
Fig. 4.
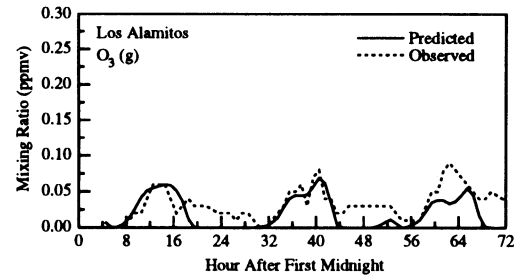
Fig. 8.
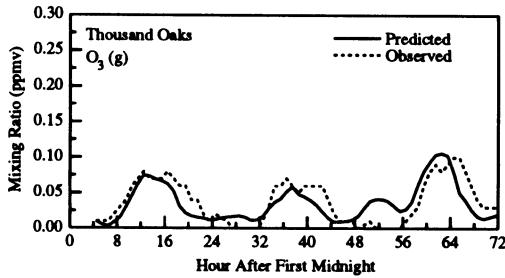
Fig. 5.
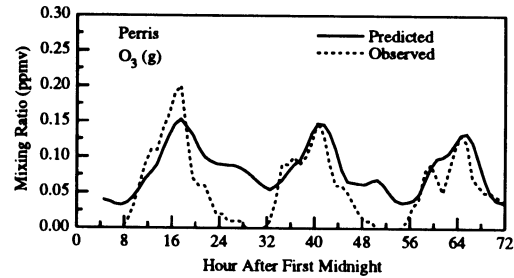
Fig. 9.
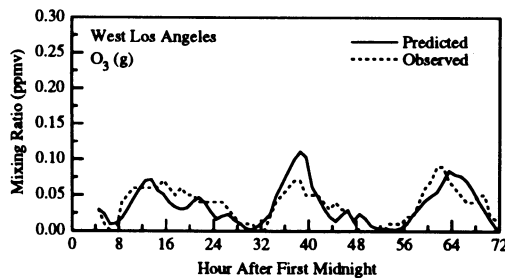
Fig. 6.
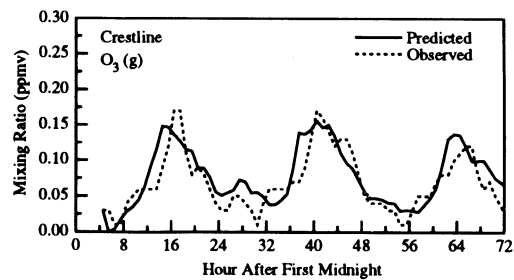
Fig. 10.

predictions were sometimes more accurate on the third day than on the second day.

Further, in some remote areas in the north- and south-eastern parts of the basin, mixing ratio predictions matched data well on the third day. For example, Figs 9, 10, and 14 show mixing ratios at Perris, Crestline, and Victorville, respectively. In all

cases, predictions on both the second and third days matched the data fairly well. Even on the first day, mixing ratio predictions at these locations were comparable to observations. In the central eastern region of the basin, such as in Fontana, San Bernardino, and Redlands (Figures 11, 12 and 13), predicted mixing ratios of ozone on the third day were lower than the
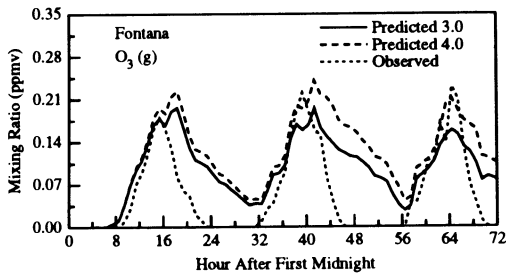
Fig. 11.
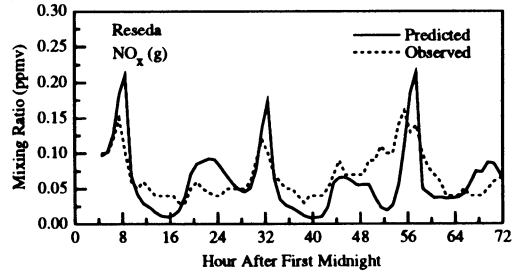
Fig. 15.
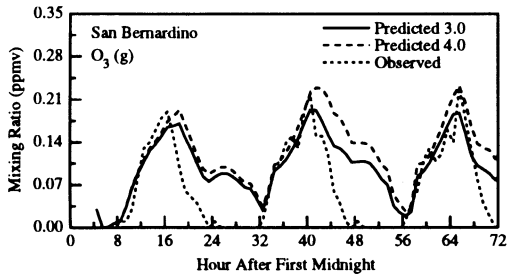
Fig. 12.
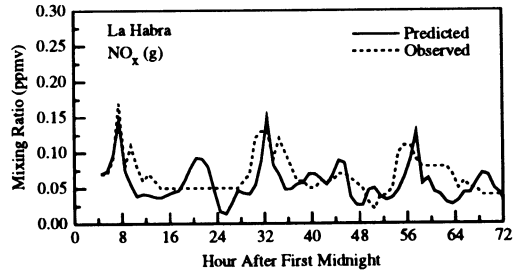
Fig. 16.
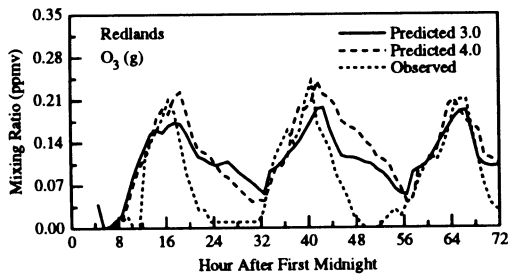
Fig. 13.
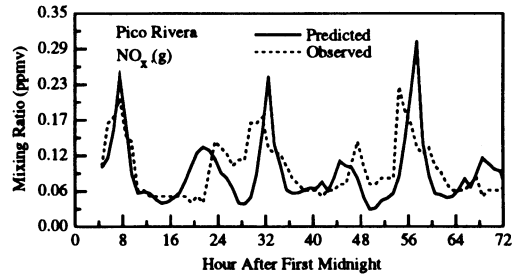
Fig. 17.
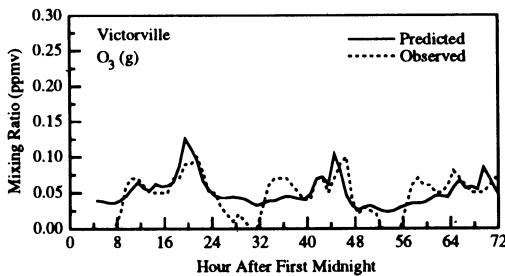
Fig. 14.
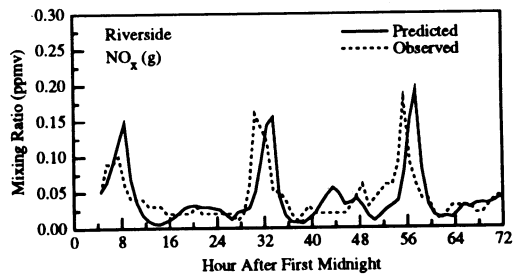
Fig. 18.

peak observed values. Sensitivity study results (same figures) show that, by increasing the multiplication factor of organic gas hot exhaust from 3.0 to 4.0, mixing ratios of ozone at these locations increased to match the peak values on the third day in all three cases.

Similarly, increasing the initial background mixing ratio of reactive organic gases in areas far beyond the eastern end of the basin helped to improve mixing ratio predictions of ozone at stations on the east end of the basin during the second and third days. Initially, organic gas mixing ratios were interpolated
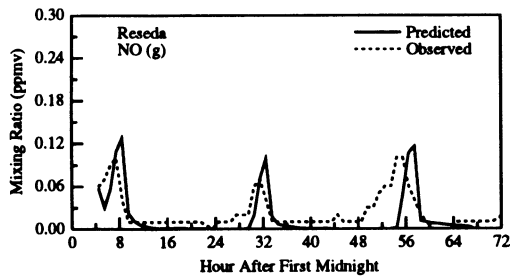
Fig. 19.
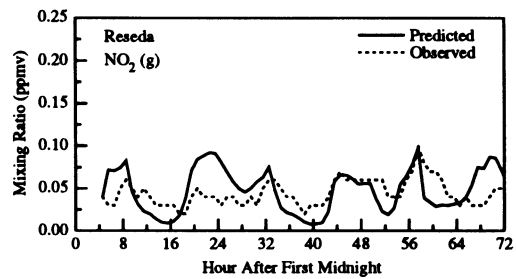
Fig. 23.
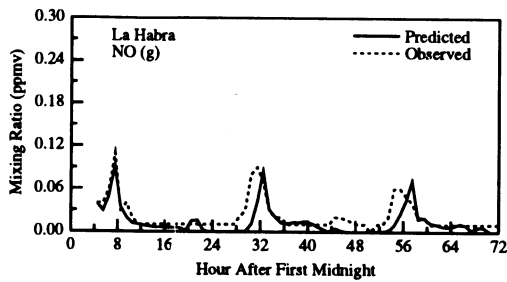
Fig. 20.
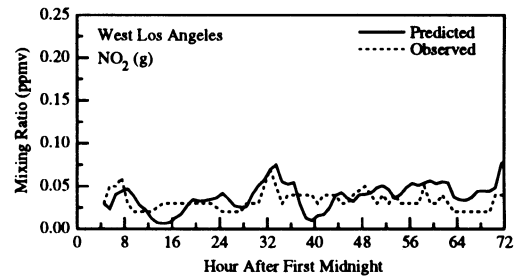
Fig. 24.
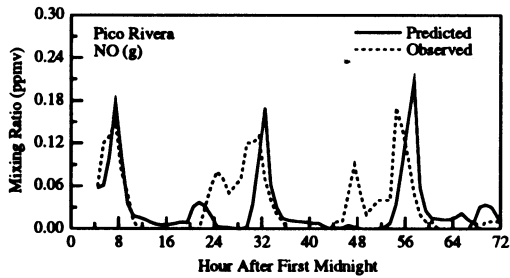
Fig. 21.
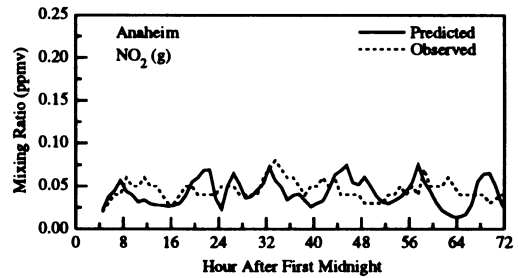
Fig. 25.
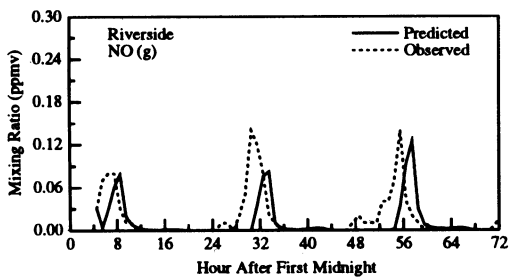
Fig. 22.
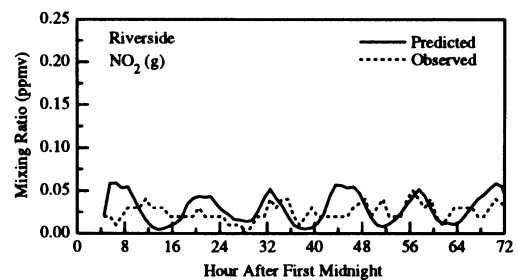
Fig. 26.

from estimated observed values, as described in Section 3.4. However, a limitation to the initialization was that only nine sites were available for interpolation (and values were taken from a different day). Thus, outside the radius of influence of the stations, mixing ratios of organic gases were initialized with unverifiable values. For the simulation and sensitivity

study results shown, organic gas mixing ratios were set to background tropospheric values for all grid cells further than 20 km from a station for which NMOC data were available. During the first day of simulation, the model performed well because organic gas mixing ratios were not significantly influenced by advective flux of air outside the region where proper
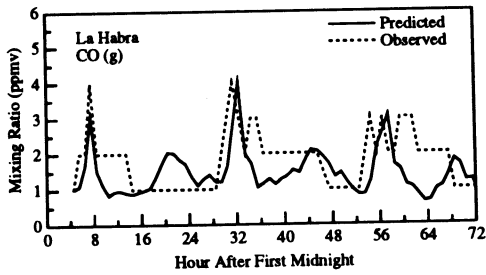
Fig. 27.
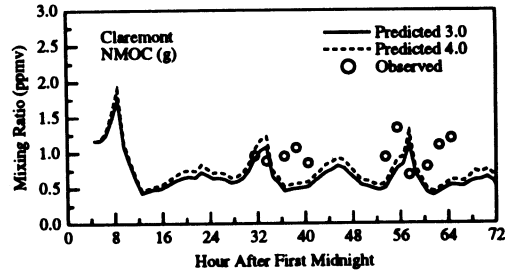
Fig. 31.
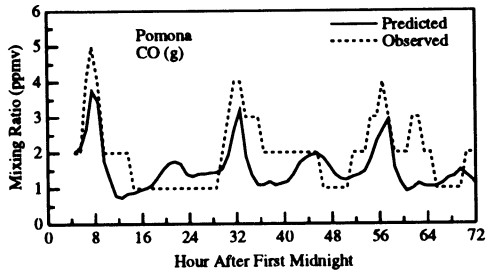
Fig. 28.
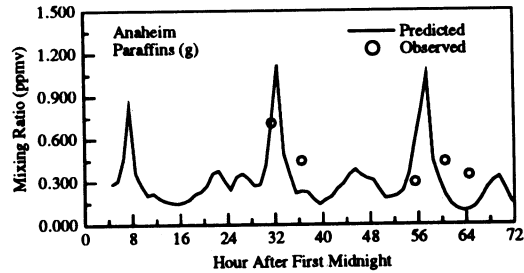
Fig. 32.
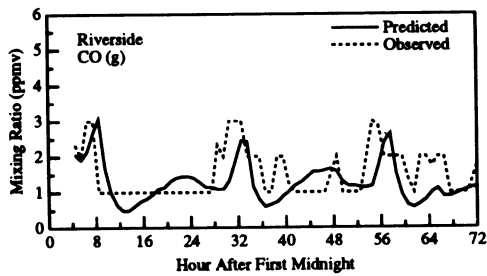
Fig. 29.
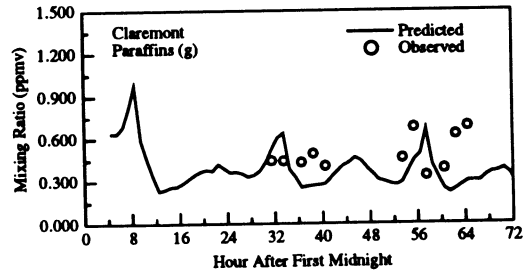
Fig. 33.
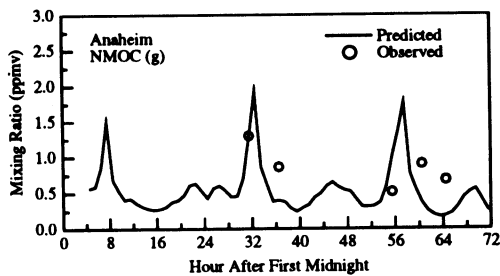
Fig. 30.
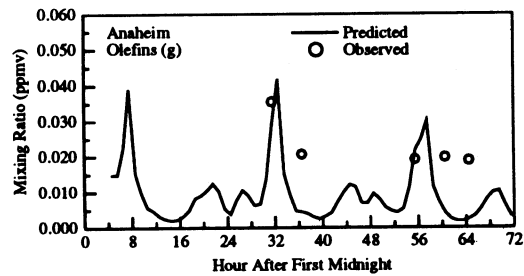
Fig. 34.

initialization occurred. On subsequent days, wind advected air to the basin from many areas on the periphery or outside the basin, where initialization was poor. Consequently, normalized gross errors in ozone increased, especially in the eastern basin.

However, by extending the "radius of influence" over land from 20 to between 30 or 60 km, ozone mixing ratio predictions on the east side of the basin improved. Such improvements, not shown here, were similar to the improvements seen in Figs 9, 10 and 14,
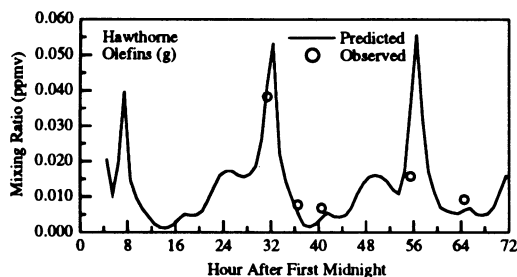
Fig. 35.
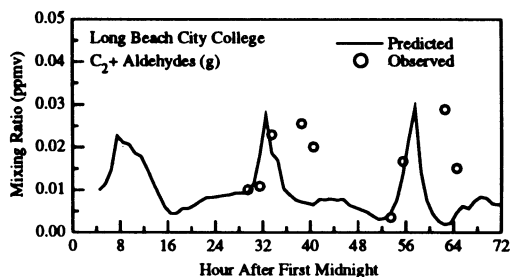
Fig. 39.
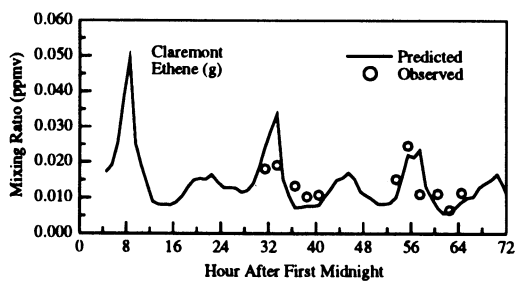
Fig. 36.
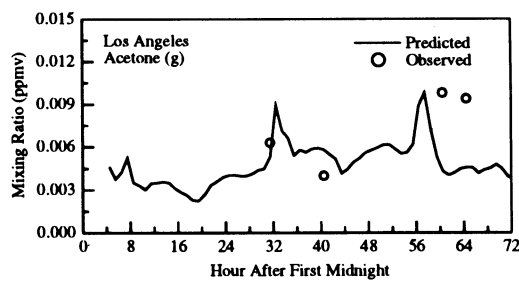
Fig. 40.
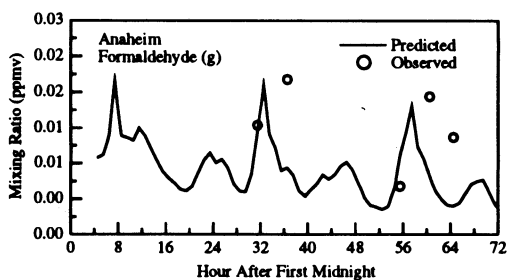
Fig. 37.
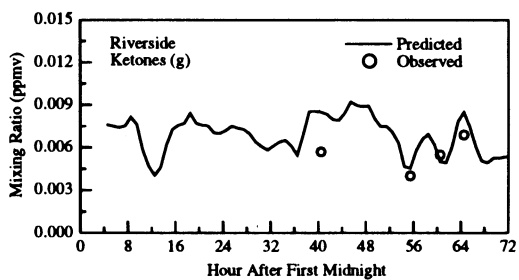
Fig. 41.
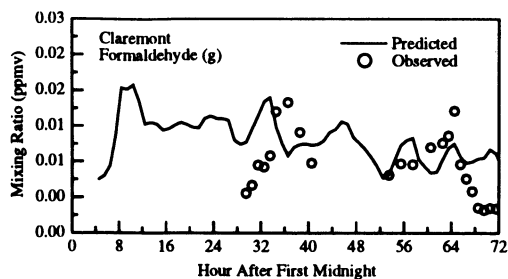
Fig. 38.
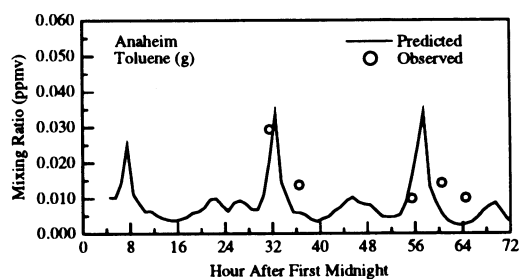
Fig. 42.

which resulted from increasing the emission factor of organic hot exhaust. The improvements were most apparent on the second and third days of simulation. Thus, both organic gas initial conditions and emissions appeared to improve simulation results.

An interesting feature of the ozone time-series plots was the presence or absence of observed nighttime ozone. Of the plots shown, observed nighttime ozone appeared in West Los Angeles, Long Beach, Los Alamitos, Crestline, and Victorville. Observed night-
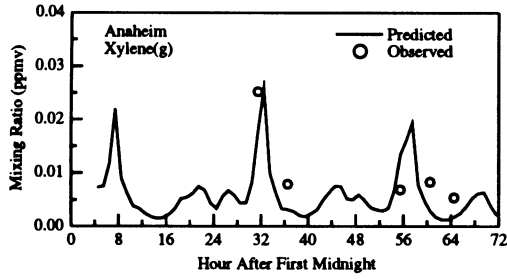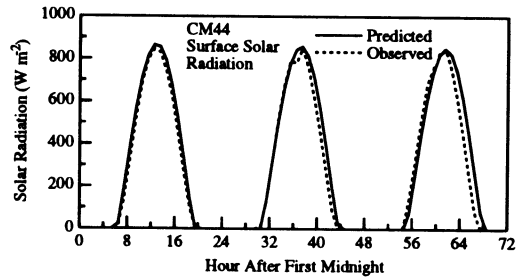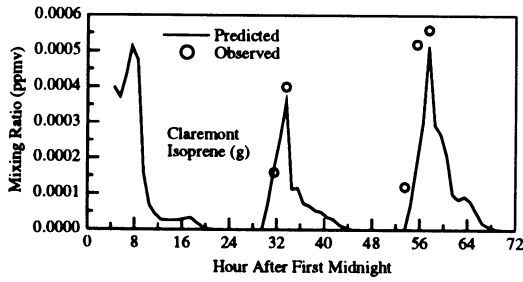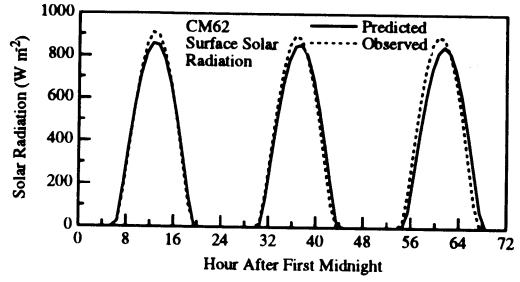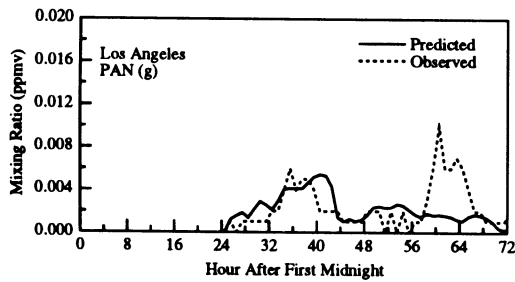
Fig. 43.

Fig. 47.

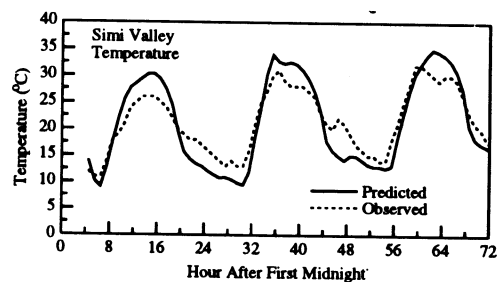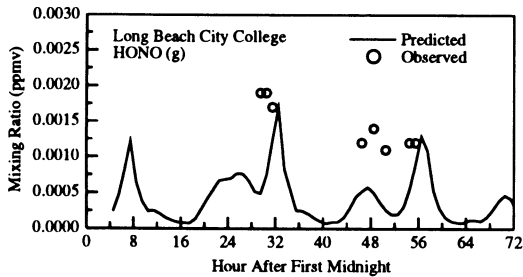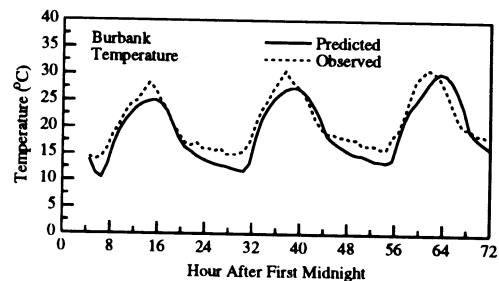Fig. 44.

Fig. 48.

Fig. 45.

Fig. 49.

Fig. 46.

Fig. 50.

time ozone was depleted, for the most part, in Simi Valley, Reseda, Thousand Oaks, Perris, Fontana, San Bernardino, and Redlands. The presence of observed nighttime ozone indicates that either ozone from aloft freely mixed down to the surface layer or that nitric

oxide was sufficiently absent near the surface. Near the coast at night, the observed atmosphere was neutral in stability, and observed nitric oxide was low. Thus, ozone from aloft was able to mix down to the surface and existing ozone near the surface was not
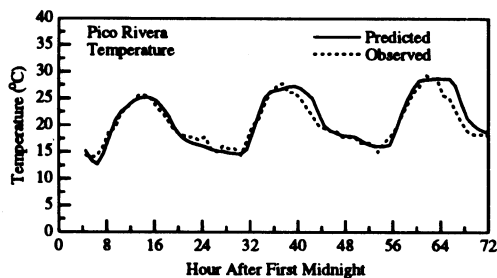
Fig. 51.
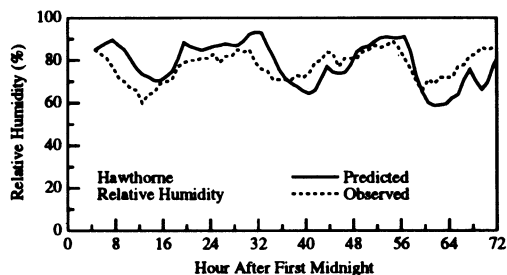
Fig. 55.
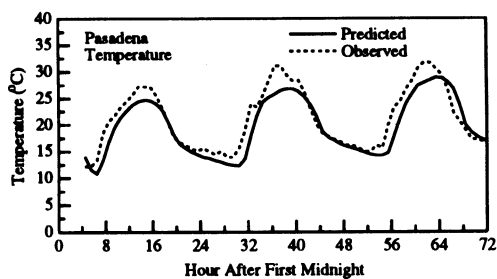
Fig. 52.
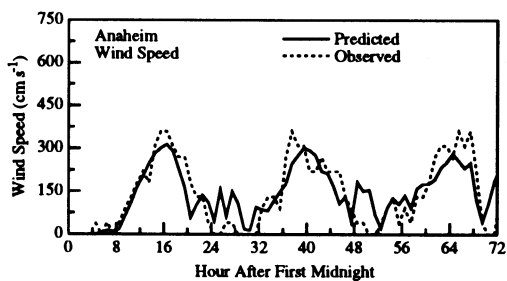
Fig. 56.
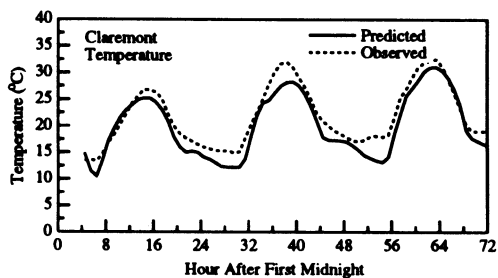
Fig. 53.
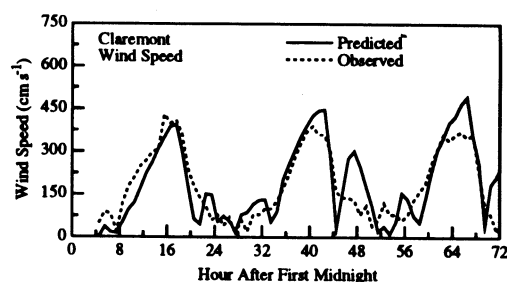
Fig. 57.
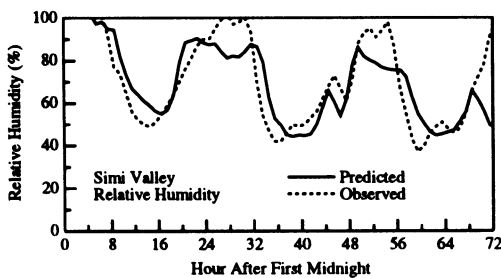
Fig. 54.
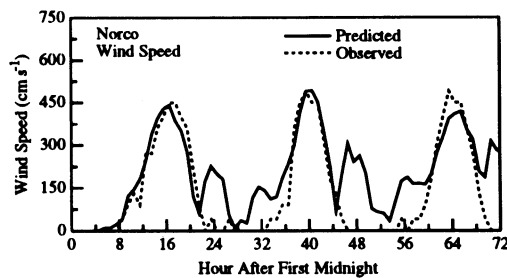
Fig. 58.

titrated by NO. To the contrary, available ozone may have depleted existing NO. In the San Fernando Valley and eastern basin, the observed atmosphere was more stable, preventing mixing of ozone aloft into the surface layer. Thus, existing NO was able to titrate remaining observed ozone near the surface.

Attempts to predict nighttime ozone mixing ratios gave mixed results. At Simi Valley, Reseda, and Thousand Oaks, the model correctly predicted ozone depletion the first night. However, simulations of the second night were less successful. At Simi Valley (Fig. 3), an observed jolt in the nighttime ozone was
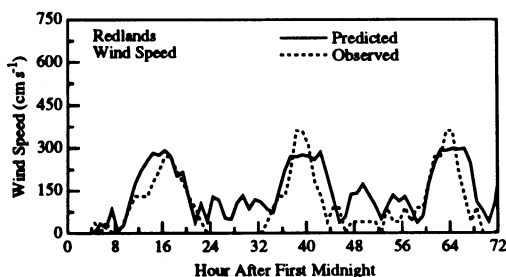
Fig. 59.
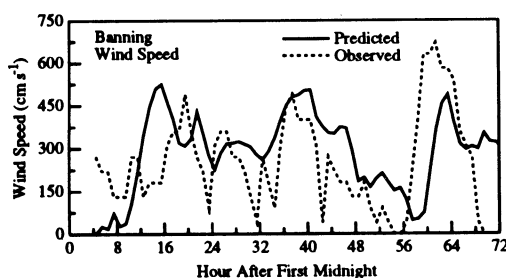
Fig. 60.

predicted, but it occurred two to three hours late and was too large. At Reseda, the model predicted a false nighttime ozone peak, and at Thousand Oaks, the model predicted an exaggerated nighttime jolt. In the eastern basin, predicted ozone was too high, probably because predicted nighttime NO was too low. Near the coast, the model predicted nighttime ozone at West Los Angeles accurately. However, at Long Beach and Los Alamitos, observed nighttime ozone was not predicted. This occurred because temperatures in the model dropped too low at these locations, increasing atmospheric stability and preventing upward mixing of nitric oxide or downward mixing of ozone. Thus, existing NO titrated ozone and ozone from aloft could not penetrate down.

The model temperature profile was predicted to be too stable because air near the surface was predicted to be too cool. Air was too cool possibly because either cool air was advected to coastal regions from the east end of the basin or the effects of nighttime fog were not included in the calculation of optical depth (these simulations included gas-phase processes only). The model tended to underpredict nighttime temperatures at many locations in the east basin; thus, cool air, carried by the land breeze, could have been advected to the coast. Nighttime temperatures were low away from the coast, possibly because soil moisture predictions were off at some locations. Such predictions depend significantly on initial soil mositure and soil characteristic data, and these data were given as averages over several landuse and soil types in each grid cell.

4.2. Oxides of nitrogen

Figures 15–18 show time-series comparisons of predicted to observed NO_x (NO + NO_2) mixing ratios. Similarly, Figs 19–22 show time-series plots of NO. As indicated by the figures, the existence of observed NO peaks were predicted each day of simulation at each location. In some cases, the times and magnitudes of the peaks were predicted correctly. In other cases, the peaks were either delayed, too high, or too low. Delays in predicted peaks appear to have been caused by a combination of emission estimate timing errors and delays in the time that the morning boundary layer was predicted to rise. Excessively high or low peaks appear to have been caused by over- or underprediction, respectively, of atmospheric stability.

First, during all three days of the emissions inventory, NO emission rates peaked between the hours of 8–9 a.m. PDT. However, on several days, the observed peaks in NO occurred before 8 a.m. Thus, slight differences in the times of estimated emissions may have caused a lag in observed NO peak mixing ratios. However, a more significant cause of predicted to observed NO mixing ratio differences may have been the timing of the morning inversion rise. If predicted mixing occurred sooner, then the peak NO mixing ratios would have occurred sooner (and would have had lower values).

The decline in NO mixing ratios after sunrise was due both to vertical diffusion and chemical reaction. The diffusion of gas from the surface layer reduced NO mixing ratios somewhat, as is evidenced by the time-series plots of carbon monoxide (Figs 27–29) and nitrogen dioxide (Figs 23–26). First, carbon monoxide and nitric oxide are emitted at similar times and from many of the same sources. However, while NO reacts significantly, CO is fairly unreactive and is a 'conserved' species (Main and Friedlander, 1990). In fact the only significant chemical loss of CO is by reaction with OH, and this reaction is moderately slow. Further, after three days of simulation, more CO was produced chemically than was destroyed by reaction with OH. The observed plots of CO show that, after about 8:00 a.m., CO mixing ratios generally declined significantly. In some cases, such as day three at La Habra, they did not. However, on day three at La Habra, NO decline was also slightly drawn out (Fig. 20). If chemical reaction were the only reason for the decline in NO mixing ratio past morning, then CO mixing ratios would not have declined at the same time.

Nevertheless, the figures for nitrogen dioxide indicate that conversion of NO to NO_2 was responsible for a significant portion of the loss of NO. For example, Fig. 19 shows that the peak observed mixing ratios of NO on each day at Reseda were about 0.10, 0.07, and 0.10 ppmv, respectively. Figure 23 shows that the peak mixing ratios of NO_2 on those three days were 0.06, 0.06, and 0.10 ppmv, respectively. Thus, a significant fraction of NO converted to NO_2 chemically.

In sum, both chemistry and vertical mixing appear to have played an important role in reducing morning NO mixing ratios. However, belated vertical mixing appears to have caused delays in predicted NO peaks near the surface. In the model, vertical diffusion was high at most locations by 8:00 a.m. on the first day of simulation. However, on the second and third days, vertical diffusion was weaker at 8:00 a.m. but stronger at 9:00 a.m. Consequently, predicted NO peaks during the first day matched observed peaks in time better than they did on the second or third days. Vertical diffusion on the second and third days was delayed because the model predicted excess stability near the surface on those days, and this was caused by excessively cold surface temperature predictions. Predictions for the first day were more accurate because the model was initialized with interpolated temperature data.

4.3. Organics and other gases

As discussed, overall ozone prediction accuracy decreased in time, possibly because organic gas and NO_x prediction accuracy decreased in time. Tables 5 and 6 show the decrease in organic gas prediction accuracy. SCAQS hourly averaged speciated organic gas data (Section 3.1) were tabulated on 27 and 28 August at 6:00, 11:00, and 15:00 PST for nine stations and additionally at 4:00, 8:00, and 13:00 PST for two stations. No data were tabulated for 26 August. Tables 5 and 6 show that the non-methane organic carbon (NMOC) gross error increased from 42.6% on 27 August to 63.2% on 28 August.

Figures 31 and 32 show time-series comparisons of total NMOC data, and Figs 33–44 show comparisons for individual organics species or groups. While NMOC prediction accuracy decreased from day two to day three, NMOCs were also generally underpredicted (e.g. Tables 4–6). A possible cause of organic gas prediction errors is an error in emissions estimates. To test the effects of emission uncertainty, the sensitivity analysis, discussed earlier, was performed. The result of increasing mobile hot exhaust organic emissions by a factor of 4.0 instead of 3.0 had little effect on the accuracy of organic predictions. For example, gross errors in NMOC predictions at 2:30 p.m., 27 and 28 August decreased from 42.6% to 38% and from 63.2% to 59.1%, respectively, when emissions were increased. Also, Fig. 31 shows that NMOC mixing ratio predictions at Claremont did not change significantly. Nevertheless, the improvement in ozone predictions at several locations was more noticeable (e.g. Figs 11–13).

Next, Figs 45 and 46 show time-series comparisons for PAN and HONO at given locations. PAN and HONO measurements (described in Section 3.1) were available for only 27 and 28 August. While PAN predictions in Los Angeles matched on the 27th, they were low on the 28th. The low predicted mixing ratios of PAN for the last day are consistent with the low predicted mixing ratios of acetaldehyde on the last

day at Los Angeles. Also, the high mixing ratio of observed PAN corresponds to the high mixing ratio of observed acetaldehyde. Conversely, predicted HONO peak mixing ratios at Long Beach were reasonable for both the 27th and 28th. However, on the 28th, HONO was observed during the nighttime whereas the model predicted its mixing ratio to peak only during the time of peak NO emissions. HONO mixing ratios were low possibly because their nighttime emissions rates were underestimated for the 28th.

4.4. Radiation and meteorological parameters

Tables 3–6 show statistics for surface solar radiation, temperature, relative humidity, wind direction, and wind speed. Also, Figs 47 and 48 show time-series plots of surface solar radiation, Figs 49–53 show plots of temperature, Figs 54 and 55 show plots of humidity, and Figs 56 and 60 show plots of wind speed. As shown in the Figs 47 and 48, predicted surface solar radiation matched observations very well (normalized gross errors during times of peak radiation were 4.4–5.2%).

Next, the normalized gross error in temperature predictions, tabulated over the 68-h simulation, was 0.8% of observed Kelvin temperatures (approximately 2.3 K). On average, temperature predictions were lower than observations, especially towards the eastern end of the basin and at night. Cool surface temperatures probably resulted from a combination of factors, including errors in soil moisture predictions and the non-inclusion of aerosols and fogs, in these particular calculations.

Humidity is dependent on both temperature and the vapor content of the air. Thus, errors in either cause errors in humidity. The normalized gross error in relative humidity, determined over the 68-h simulation period, was 24.3% and biased high. Because predicted temperatures were lower than observed temperatures, predicted humidities were expected to be too high. Humidity predictions were least accurate inland, where temperature predictions were least accurate. Near coastal regions and in the San Fernando Valley, humidity predictions were better.

Finally, the normalized gross error in wind speed, determined over the 68-h simulation period, was 74.5%. However, at times of peak wind speeds, the errors were much lower (e.g. 43.7, 39.0, and 44.0% at 2:30 p.m. on each of the three simulation days). Further, examination of several time-series plots indicates that wind speed predictions were quite reasonable during times of peak speeds, even in remote regions of the basin. For example, Fig. 60 shows that the MMTD predicted the peak wind speed magnitude and time at Banning on the second day. Also, Fig. 58 shows good predictions of wind speed at Norco on the first two days, and Fig. 56 shows good predictions at Anaheim. Thus, the MMTD was able to predict peak wind speeds both in coastal and far-inland regions. Similarly, the model predicted wind direction well

during the day. Table 3 indicates the overall gross error in wind direction was 13.6% (48°, since observed winds were normalized to 360°). However, during times of peak wind, wind direction errors averaged 8–11.1% (Tables 4–6).

4.5. Computer timing

To run the simulations discussed above, a Cray 90 computer was used. Over a grid domain of 41,800 MMTD model cells and 24,276 GATOR cells, total computational time was about 2.05 h per day of simulation at an average speed of 330 megaflops. Chemistry routines required about 72% of all computer time. In addition, the MMTD model required about 16%, radiative transfer required about 7%, horizontal and vertical transport required 4%, and setup and output routines required about 1% of the total time. Thus, chemistry was most computationally intensive. However, the dynamics and radiation modules also required significant computer time.

5. CONCLUSION

A gas, aerosol, transport, and radiation model (GATOR) was developed and coupled to the meso-scale meteorological and tracer dispersion (MMTD) model. The resulting modeling system was used to study urban and regional air pollution. GATOR simulates gas- and aqueous-phase chemistry, gas and particle emissions, deposition, transport, particle growth, evaporation, coagulation, nucleation, and chemical equilibrium. The MMTD predicts winds, diffusion, temperature, pressure, and humidity. The transport algorithms in GATOR use the predicted winds to move gases and aerosols horizontally and vertically. GATOR also calculates spectrally resolved extinction coefficients and uses a radiative transfer algorithm to calculate mean intensity and heating. The heating rates feed back to the MMTD and are used to calculate part of temperature changes.

To test the performance of all except aerosol processes acting together in an airshed model, simulations of pollution in the Los Angeles Basin were run for the SCAQS period of 26–28 August 1987. The results of a three-day simulation indicate that GATOR predicted surface ozone mixing ratios to within a gross error, normalized, over 37 monitoring stations, of 17.6% at 2:30 p.m. on the first day of simulation and 23.4% on the second day. The gross error, normalized over 307 measurements during the first 12 h of simulation, was 22%, and the gross error, normalized over 1244 d and night measurements during the entire 68-h simulation period, was 32.6%.

Time-series plots and/or statistics were also shown for nitric oxide, nitrogen dioxide, NO$_x$, carbon monoxide, total non-methane organic carbon, paraffins, olefins, ethene, formaldehyde, higher aldehydes, acetone, ketones, toluene, xylene, isoprene, peroxyacetyl nitrate, nitrous acid, methane, sulfur diox-

ide, surface solar radiation, temperature, relative humidity, wind speed, and wind direction. Such statistics and plots indicate good agreement at many locations for several parameters. In particular, surface solar radiation and temperature were predicted well. However, small errors in temperature predictions appeared to affect atmospheric stability and vertical diffusion predictions, which affected nighttime and early morning mixing ratios of many species. Another possible source of model error was the estimated emissions of organics from vehicular hot exhaust. In a sensitivity test, the hot exhaust factor for organic gases was increased from 3.0 to 4.0. This change improved but did not perfect ozone predictions inland. Also, other tests confirmed that initial mixing ratios of reactive organic gases influenced ozone mixing ratios in a similar manner as did changes in the hot exhaust emission factors.

The cases here were run on a CRAY-90 computer, and the time for all computations was about 2.05 h per 24 h of simulation. The chemistry routines took approximately 72% of all computer time.

REFERENCES

Allen P. D. and Wagner K. K. (1992) 1987 SCAQS emissions inventory, magnetic tape numbers ARA806 and ARA807. Technical Support Division, California Air Resources Board, Sacramento, California.

Ames J., Whitney D. C. and Allen P. D. (1986) Computer subroutine to calculate plume rise from Briggs formulae (1977–1986).

Atkinson R., Baulch D. L., Cox R. A., Hampson Jr R. F., Kerr J. A. and Troe J. (1992) Evaluated kinetic and photochemical data for atmospheric chemistry. Supplement IV. *J. phys. chem. Ref. Data* **21**, 1125–1571.

Bonsang B., Martin D., Lambert G., Kanakidou M., Le Roulley J. C. and Sennequier G. (1991) Vertical distribution of non methane hydrocarbons in the remote marine boundary layer. *J. geophys. Res.* **96**, 7313–7324.

Brasseur G. and Solomon S. (1986) *Aeronomy of the Middle Atmosphere*. D. Reidel, Dordrecht, Holland.

Briggs G. A. (1975) Plume rise predictions. In *Lectures on Air Pollution and Environmental Impact Analysis* (edited by Haugen D. A.), pp. 59–111. American Meteorological Society, Boston, Massachusetts.

Byrne G. D., Hindmarsh A. C., Jackson K. R. and Brown H. G. (1977) A comparison of two ODE codes: GEAR and EPISODE. *Comput. chem. Engng* **1**, 133–147.

Chang J. S., Brost R. A., Isaksen S. A., Madronich S., Middleton P., Stockwell R. and Walcek C. J. (1987) A three-dimensional Eulerian acid deposition model: Physical concepts and formulation. *J. geophys. Res.* **92**, 14,681–14,700.

Dabdub D. and Seinfeld J. H. (1994) Air quality modeling on massively parallel computers. *Atmospheric Environment* **28A**, 1679–1687.

DaMassa J., Allen P., McGuire T., McNerny D., Ranzieri A. and Wagner K. (1992) Technical Guidance Document: Photochemical Modeling. California Environmental Protection Agency/Air Resources Board.

DeMore W. B., Sanders S. P., Golden D. M., Molina M. J., Hampson R. F., Kurylo M. J., Howard C. J. and Ravishankara A. R. (1990) Chemical kinetics and photochemical data for use in stratospheric modeling. Evaluation number 9, Rep 90-1. Jet Propul. Lab., Pasadena, California.

Drummond J. W., Ehhalt D. H. and Volz A. (1988) Measurements of nitric oxide between 0–12 km altitude and 67° N to 60° S latitude obtained during STRATOZ III. J. geophys. Res. 93, 15,831–15,849.

Fiadeiro M. E. and Veronis G. (1977) On weighted-mean schemes for the finite-difference approximation to the advection–diffusion equation. Tellus 29, 512–522.

Flassak Th. and Moussiopoulos N. (1992) High resolution simulations of the sea/land breeze in Athens, Greece, using the non-hydrostatic mesoscale model MEMO. In Air Pollution Modeling and its Application IX (edited by van Dop H. and Kallos G.). Plenum Press, New York.

Gear C. W. (1971) Numerical Initial Value Problems in Ordinary Differential Equations. Prentice-Hall, Englewood Cliffs, New Jersey.

Gery M. W., Whitten G. Z., Killus J. P. and Dodge M. C. (1989) A photochemical kinetics mechanism for urban and regional scale computer modeling. J. geophys. Res. 94, 12,925–12,956.

Harley R. A., Russell A. G., McRae G. J., Cass G. R. and Seinfeld J. H. (1993a) Photochemical modeling of the Southern California Air Quality Study. Envir. Sci. Technol. 27, 378–388.

Harley R. A., Russell A. G. and Cass G. R. (1993b) Mathematical modeling of the concentrations of volatile organic compounds: Model performance using a lumped chemical mechanism. Envir. Sci. Technol. 27, 1638–1649.

Hindmarsh A. C. (1974) GEAR: ordinary differential equation system solver. Lawrence Livermore Laboratory Report UCID-30001, Rev. 3.

Hindmarsh A. C. (1983) ODEPACK, a systematized collection of ODE solvers. In Scientific Computing (edited by Stepleman R. S. et al.), pp. 55–74. North-Holland, Amsterdam.

Ingalls M. N., Smith L. R. and Kirksey R. E. (1989) Measurement of on-road vehicle emission factors in the California South Coast Air Basin. Volume I: regulated emissions. Report to the Coordinating Research Council under Project SCAQS-1. Southwest Research Institute, San Antonio, Texas.

Jacobson M. Z. (1994) Developing, coupling, and applying a gas, aerosol, transport, and radiation model to study urban and regional air pollution. Ph. D. thesis, Dept. of Atmospheric Sciences, University of California, Los Angeles.

Jacobson M. Z. and Turco R. P. (1994) SMVGEAR: A sparse-matrix, vectorized Gear code for atmospheric models. Atmospheric Environment 28A, 273–284.

Jacobson M. Z. and Turco R. P. (1995) Simulating condensational growth, evaporation, and coagulation of aerosols using a combined moving and stationary size grid. Aerosol Sci. Technol. 22, 73–92.

Jacobson M. Z., Turco R. P., Jensen E. J. and Toon O. B. (1994) Modeling coagulation among particles of different composition and size. Atmospheric Environment 28A, 1327–1338.

King D., Wheeler N. and Wagner K. (1990) Southern California Air Quality Study Modeling Data Archive. California Air Resources Board Technical Support Division, Sacramento, California.

Lawson, D. R. (1990) The Southern California air quality study. J. Air Waste Man. Ass. 40, 156–165.

Lu R. and Turco R. P. (1993) Numerical investigation of the formation of elevated pollution layers over the Los

Angeles Air Basin. Air Pollution 93 Conf. Proc., pp. 165–172. Computational Mechanics Publications.

Lu R. and Turco R. P. (1994a) Air pollutant transport in a coastal environment Part I: Two-dimensional simulations of sea-breeze and mountain effects. J. Atmos. Sci. 51, 2285–2308.

Lu R. and Turco R. P. (1994b) Air pollutant transport in a coastal environment Part II: Three dimensional simulations over the Los Angeles Basin. Atmospheric Environment (in review).

Lurmann F. W., Main H. H., Knapp K. T., Stockburger L., Rasmussen R. A. and Fung K. (1992) Analysis of the ambient VOC data collected in the Southern California Air Quality Study. Final Report to the California Air Resources Board under Contract A832-130.

Mackay G. I., Karecki D. R. and Schiff H. I. (1988) The SCAQS: tunable diode laser absorption spectrometer measurements of H_2O_2 and H_2CO at the Claremont and Long Beach "A" sites. Unisearch Associates, Concord, Ontario, Canada. Report to the California Air Resources Board under Contact A732–973.

McRae G. J. (1981) Mathematical modeling of photochemical air pollution. Ph.D. thesis, California Institute of Technology, Pasadena, California.

McRae G. J., Goodin W. R. and Senfeld J. H. (1982) Development of a second-generation mathematical model for urban air pollution—I. Model formulation. Atmospheric Environment 16, 679–696.

Main H. H. and Friedlander S. K. (1990) Dry deposition of atmospheric aerosols by dual tracer method—I. Area sources. Atmospheric Environment 24A, 103–108.

Marenco A. and Said F. (1989) Meridional and vertical ozone distribution in the background troposphere (70°N–60°S; 0–12 km altitude) from scientific aircraft measurements during the STRATOZ III experiment (June 1984). Atmospheric Environment 23, 201–214.

Marenco A., Macaigne M. and Prieur S. (1989) Meridional and vertical CO and CH_4 distributions in the background troposphere (70° N–60° S; 0–12 km altitude) from scientific aircraft measurements during the STRATOZ III experiment (June 1984). Atmospheric Environment 23, 185–200.

Morris R. E. and Myers T. C. (1990) User's guide for the Urban Airshed Model. Vol. I: User's manual for UAM (CB-IV). EPA-450/4-90-007A. U.S. Environmental Protection Agency, Research Triangle Park, North Carolina.

Moussiopoulos N., Flassak Th. and Kessler Ch. (1992) Modelling of the photosmog formation in Athens. In Air Pollution Modeling and its Application IX (edited by van Dop H. and Kallos G.). Plenum Press, New York.

Nautical Almanac Office and Her Majesty's Nautical Almanac Office (1993) Astronomical Almanac. U.S. Government Printing Office, Washington, District of Columbia.

NASA (1990) TOMS gridded ozone data (1978–1988). NASA Upper Atmosphere Research Program, Goddard Ozone Processing Team.

Paulson S. E. and Seinfeld J. H. (1992) Development and evaluation of a photooxidation mechanism for isoprene J. geophys. Res. 97, 20,703–20,715.

Pepper D. W., Kern C. D. and Long P. E. Jr. (1979) Modeling the dispersion of atmospheric pollution using cubic splines and chapeau functions. Atmospheric Environment 13, 223–237.

Pierson W. R., Robinson N. F. and Gertler A. W. (1992) Review and reconciliation of on-road emission factors in the SoCAB. Southern California Air Quality Study Data Analysis Conference Proceedings, AWMA, Pittsburgh Pennsylvania.

Pilinis C. and Seinfeld J. H. (1988) Development and evaluation of an Eulerian photochemical gas-aerosol model. Atmospheric Environment 22, 1985–2001.

Press W. H., Flannery B. P., Teukolsky S. A. and Vetterling W. T. (1993) Numerical Recipes: The Art of Scientific Computing. Cambridge University Press, Cambridge.

Reynolds S. D., Roth P. M. and Seinfeld J. H. (1973) Mathematical modeling of photochemical air pollution—I: Formulation of the model. *Atmospheric Environment* **7**, 1033–1061.

Reynolds S. D., Liu M. K., Hecht T. A., Roth P. M. and Seinfeld J. H. (1974) Mathematical modeling of photochemical air pollution—III: Evaluation of the model. *Atmospheric Environment* **8**, 563–596.

Roth P. M., Reynolds S. D., Roberts P. J. W. and Seinfeld J. H. (1971) Development of a simulation model for estimating ground-level concentrations of photochemical pollutants. Systems Applications Inc., San Rafael, California (SAI 71/21).

Roth P. M., Roberts P. J. W., Liu M. K., Reynolds S. D. and Seinfeld J. H. (1974) Mathematical modeling of photochemical air pollution—II: A model and inventory of pollutant emissions. *Atmospheric Environment* **8**, 97–130.

Russell A. G., McCue K. F. and Cass G. R. (1988a) Mathematical modeling of the formation of nitrogen-containing air pollutants. 1. Evaluation of an Eulerian photochemical model. *Envir. Sci. Technol.* **22**, 263–271.

Russell A. G., McCue K. F. and Cass G. R. (1988b) Mathematical modeling of the formation of nitrogen-containing air pollutants 2. Evaluation of the effect of emission controls. *Envir. Sci. Technol.* **22**, 1336–1347.

Russell A. G., Winner D. A., Harley R. A., McCue K. F. and Cass G. R. (1993) Mathematical modeling and control of the dry deposition flux of nitrogen-containing air pollutants. *Envir. Sci. Technol.* **27**, 2772–2782.

Scheffe R. D. and Morris R. E. (1993) A review of the development and application of the Urban Airshed Model. *Atmospheric Environment* **27B**, 23–39.

Seinfeld J. H. (1986) *Atmospheric Chemistry and Physics of Air Pollution.* Wiley, New York.

Sheih C. M., Wesely M. L. and Walcek C. J. (1986) A dry deposition module for regional acid deposition. EPA/6000/3-86/037. U.S. Government Printing Office, Washington, District of Columbia.

Sherman A. H. and Hindmarsh A. C. (1980) GEARS: a package for the solution of sparse, stiff ordinary differential equations. Lawrence Livermore Laboratory Report UCRL-84102.

Singh H. B., Viezee W. and Salas L. J. (1988) Measurements of selected C_2–C_5 hydrocarbons in the troposphere: Latitudinal, vertical, and temporal variations. *J. geophys. Res.* **93**, 15,861–15,878.

Tesche T. W. (1988) Accuracy of ozone air quality models. *J. Envir. Engng* **114**, 739–752.

Toon O. B., Turco R. P., Westphal D., Malone R. and Liu M. S. (1988) A multidimensional model for aerosols: Description of computational analogs. *J. Atmos. Sci.* **45**, 2123–2143.

Toon O. B., McKay C. P. and Ackerman T. P. (1989) Rapid calculation of radiative heating rates and photodissociation rates in inhomogeneous multiple scattering atmospheres. *J. geophys. Res.* **94**, 16,287–16,301.

Turco R. P., Hamill P., Toon O. B., Whitten R. C. and Kiang C. S. (1979) A one-dimensional model describing aerosol formation and evolution in the stratosphere. Part I: Physical processes and mathematical analogs. *J. Atmos. Sci.* **36**, 699–717.

U.S. Department of the Army (1958) Universal Transverse Mercator grid. Tables for transformation of coordinates from grid to geographic: Clarke 1866 Spheroid. U.S. Government Printing Office, Washington, District of Columbia.

Wakimoto R. M. and McElroy J. L. (1986) Lidar observations of elevated pollution layers over Los Angeles. *J. Clim. appl. Met.* **25**, 1583–1599.

Walcek C. J., Brost R. A., Chang J. S. and Wesely M. L. (1986) SO_2, sulfate, and HNO_3 deposition velocities computed using regional landuse and meteorological data. *Atmospheric Environment* **20**, 949–964.

William E. L. II and Grosjean D. (1989) SCAQS: peroxyacetyl nitrate (PAN) measurements. Daniel Grosjean and Associates, Inc., Ventura, CA. Report to the California Air Resources Board under contract A6-099-32.

Winer A. M. and Biermann H. W. (1994) Long pathlength differential optical absorption spectroscopy (DOAS) measurements of gaseous HONO, NO_2 and HCHO in the California south coast air basin. *Res. Chem. Intermed.* **20**, 423–445.

Winer A. M., Biermann H. W., Dinoff T., Parker L. and Poe M. P. (1989) Measurements of nitrous acid, nitrate radicals, formaldehyde and nitrogen dioxide for the SCAQS by differential Optical Absorbtion Spectroscopy. Statewide Air Pollution Research Center, University of California, Riverside, California Report to the California Air Resources Board under Contract A6-146-32.

Yamartino R. J., Scire J. S., Carmichael G. R. and Chang Y. S. (1992) The CALGRID mesoscale photochemical grid model—I. Model formulation. *Atmospheric Environment* **26A**, 1493–1512.